Influence of the anisotropic hyperfine interaction on the ^{14}N ENDOR and the ESEEM orientation-disordered spectra

Nikolas P. Benetis [a],*, Sergei A. Dikanov [b]

[a] *Institute of Organic and Pharmaceutical Chemistry, Laboratory of Molecular Analysis, National Hellenic Research Foundation, EIE, Vas. Konstantinou str. 48, Athens GR-116 35, Greece*
[b] *Department of Veterinary Clinical Medicine, University of Illinois, Urbana IL 61801, USA*

Abstract

The influence of the anisotropic hyperfine interaction on the ^{14}N electron-nuclear double resonance/electron spin echo envelope modulation spectra is studied by approximate *analytical* and *graphical* methods for the case of the isotropic $\boldsymbol{g}$-factor. The suggested determination of the *modified characteristic directions* of the magnetic field due to anisotropy enhances the insight in the structural details of the system and analytical solutions of the secular equation for these conditions are derived. The graphical method, previously used for the analysis of the orientation dependence of the ^{14}N nuclear-transition frequencies in orientation-disordered samples for isotropic hyperfine interaction is extended to the case of arbitrary anisotropic hyperfine tensor. The above analytical and graphical methods are illustrated and tested against exact simulations in two practically important cases: (i) isotropic hyperfine interaction (hfi) exceeding other nuclear interactions in nuclear spin Hamiltonian. (ii) Cancellation of the isotropic part of the hfi.
© 2005 Elsevier Inc. All rights reserved.

Keywords: Orientation-disorder; ^{14}N ENDOR/ESEEM frequencies; Graphical approach; Anisotropic hfi; Double-quantum transition; Isotropic hfi cancellation

1. Introduction

High-resolution EPR techniques, such as electron-nuclear double resonance (ENDOR) and one- and two-dimensional electron spin echo envelope modulation (ESEEM), are very sensitive and informative for structural studies of the paramagnetic species and their environment in amorphous solids. They find wide applicability in structural biochemistry [1–5] due to their ability to characterize metal ligands or the interaction of radical species with their environment in proteins prepared in frozen solutions of limited concentration, and do not require growth of single crystals. An important motif in protein studies is the nitrogen ^{14}N ligation of the metal centers or its participation in the formation of hydrogen bonds with paramagnetic species. Magnetic resonance techniques provide information about the chemical type of nitrogen and its structural characteristics based on the hyperfine and quadrupole couplings determined from powder or orientation-selected spectra [1–5].

The solution of the time-independent Schrödinger equation for an electronic triplet with large zero field splitting (ZFS) or a ^{14}N nuclear spin $I = 1$ with large nuclear quadrupole interaction (nqi) are mathematically equivalent and reduce to the solution of a secular equation of third degree with respect to the eigenfrequencies. The corresponding mathematical problem of diagonalizing a 3×3 complex Hermitian matrix is analytically solvable and was applied by Muha [6,7] for the computation of the eigenvalues and the eigenvectors of the nuclear spin Hamiltonian of ^{14}N with arbitrary nqi tensor in the presence of a static magnetic field, applied to nuclear quadrupole resonance (nqr). This approach can be

---

* Corresponding author. Fax: +30 210 727 38 31.
E-mail address: niben@eie.gr (N.P. Benetis).

extended on the more general case including arbitrary *g*-, hyperfine-**A** and nuclear quadrupole tensors **Q**.

However, the complete interpretation of the spectral features present in ^{14}N powder spectra and exact determination of the hyperfine and quadrupole tensors requires usually time consuming numerical simulations. The complexity of analysis would increase proportionally if the tensors of several nuclei need to be determined from experimental nuclear frequencies. In that situation, the development of approximate approaches providing an immediate estimate of part of the required parameters directly from the spectra are highly desirable.

Dikanov et al. [8,9] have proposed a *graphical method* to explore the dependence of the ^{14}N nuclear frequencies on the *isotropic* hyperfine constant and the nqi parameters. The same method was previously used by Kottis and Lefebvre [10] in simulations of CW-EPR powder spectra of triplets with substantial ZFS. This method has the advantage to give important semi-quantitative information about the orientational properties of the transition frequencies without actually requiring the solution of the secular equation. Flanagan and Singel [11] extended this approach and analyzed in detail the spectral features of one-dimensional ^{14}N ESEEM spectra for isotropic hyperfine interaction (hfi) combining the graphical approach with simulations of the spectra. Some additional characteristics of the powder ^{14}N spectra for the isotropic hfi were established by Lee et al. [12], while Maryasov and Bowman [13] have recently reported the theoretical consideration of the ^{14}N HYSCORE spectra for the same case.

Although the results of these works facilitate the understanding of the ^{14}N spectra and the estimation of the hyperfine and quadrupole couplings, the influence of the anisotropic hfi on the characteristic features of powder spectra requires better qualitative and quantitative understanding. In spite that the solution of the secular equation is analytically available its mathematical complexity does not permit any insight to the resulting spectral features because the use of the even more complicated eigenfunctions is required. The situation becomes hopeless when polyoriented samples are considered. Therefore, in the present work we used accurate analytical simulations of ENDOR and ESEEM spectra to compare to new approximate *analytical* and *graphical* treatments studying the influence of the anisotropy directly on the *nuclear sublevel transitions*. The aim was to adapt the graphical method to the *anisotropic* case, both for the hfi and/or for the electron Zeeman interaction, for practical use in single crystals and powders. This was achieved by taking simpler theoretical detours available by the graphical method. Thus, the *modified characteristic directions* for non-coinciding **Q** and **A** tensors were first determined. From these results, analytical expressions of the *dq* transitions and the *stationary points* of the transition frequencies were derived.

Finally, explicit relations of the total span of the ENDOR and the stimulated ESEEM spectra and the positions and the inhomogeneous broadening of the characteristic features of the powder spectra in certain powders were also obtained analytically.

2. Sublevel spin Hamiltonian

Assuming high field conditions, the magnetic energy of a nucleus I, coupled to an electron spin S in the $M(\equiv M_S)$ sublevel, is given by the effective *nuclear sublevel* Hamiltonian, [14].

$$H_{I;M} = H_{I;M}^{\text{hfi}} + H_{I;M}^{\text{nZee}} + H_I^{\text{nqi}} = h\mathbf{I}^+ \cdot \mathbf{v}_{I;M} + \mathbf{I}^+ \cdot \mathbf{Q} \cdot \mathbf{I}. \quad (1)$$

Expressing the nuclear spin operator **I** in Cartesian coordinates $\mathbf{U} = (X, Y, Z)$, which coincide with the principal directions of the nqi tensor, the Eq. (1) becomes:

$$H_{I;M} = h[I_X v_{I;M}^{(X)} + I_Y v_{I;M}^{(Y)} + I_Z v_{I;M}^{(Z)}] - K[(1 - \eta)I_X^2 \\ + (1 + \eta)I_Y^2 - 2I_Z^2]. \quad (2)$$

This expression contains the Cartesian components $v_{I;M}^{(U)}$ of the vector $\mathbf{v}_{I,M}$, which will further be called effective nuclear sublevel frequency (ENSF) vector. The term ENSF refers to the degenerate single quantum (*sq*) ENDOR transition-frequencies between the nuclear states of each manifold in the absence of quadrupole [14]. Also the quadrupole strength $K = Q_{zz}/2$, and the asymmetry parameter, $\eta = (Q_{xx} - Q_{yy})/Q_{zz}$ appear in the above relations.

The *sublevel Hamiltonian* has the following matrix representation:

$$
\begin{array}{cccc}
 & |X\rangle & |Y\rangle & |Z\rangle \\
\langle X| & K(1 - \eta) & -iv_{I;M}^{(Z)} & -iv_{I;M}^{(Y)} \\
\langle Y| & iv_{I;M}^{(Z)} & K(1 + \eta) & -iv_{I;M}^{(X)} \\
\langle Z| & iv_{I;M}^{(Y)} & iv_{I;M}^{(X)} & -2K
\end{array} \rightarrow \mathbf{H}_{\text{tot}}(M)
$$

$$= K \begin{pmatrix} 1 - \eta & -i\tilde{v}_{I;M}^{(Z)} & -i\tilde{v}_{I;M}^{(Y)} \\ i\tilde{v}_{I;M}^{(Z)} & 1 + \eta & -i\tilde{v}_{I;M}^{(X)} \\ i\tilde{v}_{I;M}^{(Y)} & i\tilde{v}_{I;M}^{(X)} & -2 \end{pmatrix} \quad (3)$$

in the standard basis

$$\left\{ |X\rangle = \frac{1}{\sqrt{2}}[|-1\rangle - |1\rangle], \right.$$

$$\left. |Y\rangle = \frac{i}{\sqrt{2}}[|-1\rangle + |1\rangle] \text{ and } |Z\rangle = |0\rangle. \right\} \quad (3a)$$

The diagonal matrix elements are the pure quadrupole eigenfrequencies $\lambda_X = (1 - \eta)K$, $\lambda_Y = (1 + \eta)K$, and $\lambda_Z = -2K$ corresponding to $|X\rangle$, $|Y\rangle$, and $|Z\rangle$, respectively. The off-diagonals contain *reduced* ENSF vector components as they are divided by K

$$\tilde{v}_{I;M}^{(U)} = \frac{v_{I;M}^{(U)}}{K} \quad \text{for } U = X, Y, Z. \quad (4)$$

Thus, the problem of finding the sublevel frequencies in the case of the ^{14}N with spin $I = 1$ coupled to an electron spin doublet, finally leads to solving the following secular equation of third degree for the eigenfrequencies λ.

$$\lambda^3 - [\tilde{v}_{I;M}^2 + \eta^2 + 3]\lambda + \tilde{v}_{I;M}^2 - 3(\tilde{v}_{I,M}^{(Z)})^2$$
$$+ \eta\left[(\tilde{v}_{I,M}^{(Y)})^2 - (\tilde{v}_{I,M}^{(X)})^2\right] + 2(1 - \eta^2) = 0. \tag{5}$$

One can introduce the coefficient p_M of the linear term, and the "constant" coefficient q_M of the secular equation (the quadratic term is missing in this equation).

$$p_M \equiv p_M(\vartheta, \varphi; \Omega_g, \Omega_A) = \tilde{v}_{I;M}^2 + \eta^2 + 3, \tag{6}$$

$$q_M = -\left\{\tilde{v}_{I;M}^2 - 3(\tilde{v}_{I,M}^{(Z)})^2 + \eta\left[(\tilde{v}_{I,M}^{(Y)})^2 - (\tilde{v}_{I,M}^{(X)})^2\right] + 2(1 - \eta^2)\right\}. \tag{7}$$

Then, the secular equation obtains the implicit form appropriate to be solved by the analytical method of Muha [6,7].

$$\lambda^3 - p_M\lambda - q_M = 0. \tag{8}$$

The eigenvalues and the eigenvector of the sublevel nuclear-spin Hamiltonians are well studied and used previously for the calculation of the frequencies and intensities of the ENDOR/ESEEM transitions and simulation of the spectra [5,6,12].

3. Properties of the effective nuclear sublevel frequency vectors

The quantities of the spin system that critically influence the solution of Muha equation are the ENSF vectors and their components. The general definition for the ENSF vector $\mathbf{v}_{I;M}$ is [14,15]

$$\mathbf{v}_{I;M} = \left[\frac{M}{g'}\mathbf{A} \cdot \mathbf{g}^+ + v_{0I}\mathbf{E}\right] \cdot \mathbf{b} \equiv \mathbf{G}_M \cdot \mathbf{b}. \tag{9}$$

The matrix $\mathbf{G}_M$ is the effective nuclear sublevel (ENS) g-*tensor* as it plays an analogous role to the NMR *chemical shift anisotropy* tensor. Here, the nuclear spin can be affected strongly by the hfi, and in addition it gives different $\mathbf{G}_M$ tensors in the two electronic sublevels $M = \pm1/2$.

The direction of $\mathbf{v}_{I;M}$ signifies the quantization axis of the nuclear spin in the sublevel manifold M. The unit vector $\mathbf{b}(\vartheta, \varphi) = (\sin\vartheta \cos\varphi, \sin\vartheta \sin\varphi, \cos\vartheta)^+$ stands for the *direction* of the magnetic field $\mathbf{B}_0 = B_0 \mathbf{b}$, as it can be expressed by the spherical polar angles, ϑ and φ.

The nuclear Zeeman frequency v_{0I} is given by $v_{0I} = -\gamma_I B_0/2\pi$.

The value of the effective g-factor $g' \equiv g'(\vartheta, \varphi)$ is generally orientation dependent according to the following equation:

$$g'(\vartheta, \varphi; \Omega_g) = \left|\mathbf{g}(\Omega_g)^+ \cdot \mathbf{b}(\vartheta, \varphi)\right| \equiv \sqrt{\mathbf{b}^+ \cdot \mathbf{g}^2 \cdot \mathbf{b}}. \tag{10}$$

The Euler angles Ω_g determine the orientation of the g-tensor in preselected coordinate system.

Notice that even though the above $\mathbf{g}$ and $\mathbf{A}$ tensors are real and symmetric, it can be easily shown that the matrix $\mathbf{G}_M$ is real but not necessarily symmetric. This problem pops-up when both $\mathbf{g}$ and $\mathbf{A}$ are anisotropic and therefore the consequences of it were not further studied in this work as they do not either appear to influence the numerical simulation of the spectra.

The magnitudes of the ENSF's for $M = \alpha, \beta$ are given by defining their squares.

$$v_{I;M}^2 = \mathbf{b}^+ \cdot \mathbf{G}_M^+ \cdot \mathbf{G}_M \cdot \mathbf{b}. \tag{11}$$

The matrix product of $\mathbf{G}_M$ in the middle of the above equation, which is back again a symmetric matrix, is as follows:

$$\mathbf{G}_M^+ \cdot \mathbf{G}_M = \frac{M^2}{g'^2}\mathbf{g} \cdot \mathbf{A}^2 \cdot \mathbf{g} + \frac{M}{g'}v_{0I}(\mathbf{g} \cdot \mathbf{A} + \mathbf{A} \cdot \mathbf{g}) + v_{0I}^2\mathbf{E}. \tag{12}$$

Analytical expressions could be derived for a general matrix $\mathbf{G}_M$ in this work provided that the orientation of the $\mathbf{g}$- and $\mathbf{A}$-tensors are both known in the same frame of reference, here the nqi principal system $\mathbf{U} \equiv (\mathbf{X}, \mathbf{Y}, \mathbf{Z})$. The frame $\mathbf{U}$ is used as a common frame of reference for the entire system, including field direction. The Euler angles Ω_g and Ω_A, which specify the orientation of the $\mathbf{g}$- and $\mathbf{A}$-tensors in the frame $\mathbf{U}$, respectively, are part of the necessary input, see further for definitions. The case where only the $\mathbf{A}$-tensor is anisotropic is analytically tractable and will be analyzed carefully in the present work.

Generally, the Cartesian tensor $\mathbf{A}$ is a full 3×3 real matrix when expressed in a frame other than its own principal frame, as specified by the following transformation:

$$\mathbf{A} = \mathbf{R} \cdot \mathbf{A}^D \cdot \mathbf{R}^+, \tag{13}$$

where $\mathbf{R} \equiv \mathbf{R}(\Omega_A)$ is the active rotation of the diagonal tensor $\mathbf{A}^D$ from its principal frame to the $\mathbf{U}$-frame, specified by the columns of $\mathbf{R}$. This rotation is determined conventionally by the Euler angles $\Omega_{QA} = (\alpha_{QA}, \beta_{QA}, \gamma_{QA})$ for the inverse rotation of the above frames, [16]. The notation of the Euler angles is in this text simplified to $\Omega_A = (\alpha_A, \beta_A, \gamma_A)$.

The components of the vector $\mathbf{v}_{I;M}$ in the $\mathbf{U}$-frame could be expressed analytically as functions of relatively few parameters, i.e., the *parallel* and the *perpendicular anisotropies*, proportional to T_{zz} and $T_{xx} - T_{yy}$ of $\mathbf{A}$ tensors, respectively, and the Euler angles Ω_A, see Appendix A. The best way to proceed is to present the explicit expressions of the matrix elements of $\mathbf{G}_M$. First, the diagonal elements of the ENS $\mathbf{G}_M$-tensor in the nqi frame for isotropic $\mathbf{g}$-tensor are summarized.

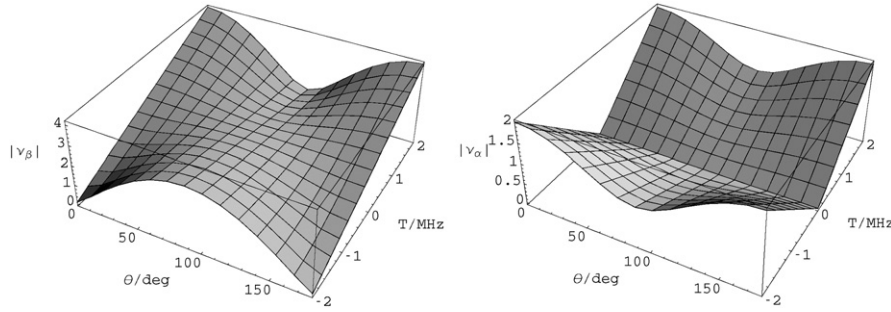$$G_M^{(XX)} = M\{a - \tfrac{1}{2}[T_{ZZ} - (T_{XX} - T_{YY})]\} + v_{0I}, \tag{14a}$$

Fig. 1. The value of the ENS frequencies (reduced by K) as a function of the polar angle ϑ of the field orientation and the hfi anisotropy T. This figure was obtained for axial $\mathbf{A}$ coinciding with the $\mathbf{Q}$ tensors ($\mathbf{g}$-isotropic). The scalar part of the hf coupling $a = 2.0848$ MHz was kept constant. The other parameters were: $\eta = 0.47$, and $K = 1.4$ MHz ($v_{0I} = -1.06$ MHz close to cancellation of a). The explicit relation in Eq. (B.9) was used for this plot.

$$G_M^{(YY)} = M\{a - \tfrac{1}{2}[T_{ZZ} + (T_{XX} - T_{YY})]\} + v_{0I}, \qquad (14b)$$

$$G_M^{(ZZ)} = M(a + T_{ZZ}) + v_{0I} \qquad (14c)$$

with,

$$T_{ZZ} = \tfrac{1}{2}[T_{zz}(3\cos^2\beta - 1) + (T_{xx} - T_{yy})\cos(2\alpha)\sin^2\beta], \qquad (15a)$$

$$\begin{aligned} T_{XX} - T_{YY} = {} & \tfrac{3}{2}\sin^2\beta \, T_{zz}\cos(2\gamma) + (T_{xx} - T_{yy}) \\ & \times \{\sin^4(\beta/2)\cos[2(\alpha - \gamma)] \\ & + \cos^4(\beta/2)\cos[2(\alpha + \gamma)]\}. \end{aligned} \qquad (15b)$$

The Cartesian components of $\mathbf{T}$ with the capital indices X, Y, and Z are meant in the $\mathbf{Q}$-principal frame $\mathbf{U}$, while the Cartesian components in lower-case indices x, y, and z are meant in the $\mathbf{A}$-principal frame. If the tensor components T_{XX}, T_{YY} are required separately one can use a combination of Eq. (15b) with $T_{XX} + T_{YY} = -T_{ZZ}$.

The off-diagonal elements of the $\mathbf{G}_M$ matrix in the $\mathbf{U}$-frame are given by:

$$G_M^{(I;J)} = MT_{I;J} \quad \text{with} \quad I, J = X, Y, Z; \; I \neq J. \qquad (16)$$

Their relations to the components of the tensor $\mathbf{A}$ in its own principal frame are given by:

$$\begin{aligned} T_{XY} = {} & -\tfrac{3}{4}T_{zz}\sin^2\beta \sin(2\gamma) - \tfrac{1}{2}(T_{xx} - T_{yy}) \\ & \times \{\cos^4(\beta/2)\sin[2(\alpha + \gamma)] \\ & - \sin^4(\beta/2)\sin[2(\alpha - \gamma)]\}, \end{aligned} \qquad (17a)$$

$$\begin{aligned} T_{YZ} = {} & \tfrac{3}{4}T_{zz}\sin(2\beta)\sin\gamma - \tfrac{1}{2}(T_{xx} - T_{yy}) \\ & \times \sin\beta[\sin(2\alpha)\cos\gamma + \cos(2\alpha)\cos\beta\sin\gamma], \end{aligned} \qquad (17b)$$

$$\begin{aligned} T_{ZX} = {} & \tfrac{3}{4}T_{zz}\sin(2\beta)\cos\gamma + \tfrac{1}{2}(T_{xx} - T_{yy}) \\ & \times \sin\beta[\sin(2\alpha)\sin\gamma - \cos(2\alpha)\cos\beta\cos\gamma]. \end{aligned} \qquad (17c)$$

Recalling the typical symmetry of the $\mathbf{A}$-tensor $A_{ij} = A_{ji}$, all the needed matrix elements are already taken into account by considering only the above five Eqs. (15a), (15b) and (17a)–(17c).

The length of ENS vector is

$$\begin{aligned} |\mathbf{v}_{I;M}| &= \sqrt{[v_{I,M}^{(X)}]^2 + [v_{I,M}^{(Y)}]^2 + [v_{I,M}^{(Z)}]^2} \\ &\equiv \sqrt{v_X^2 + v_Y^2 + v_Z^2}. \end{aligned} \qquad (18)$$

(The last identity is a simplified notation omitting the M dependence of the Cartesian components of the $\mathbf{v}_{I;M}$ vector.) The length of the ENSF vector fulfills the typical relation to its components in any coordinate system but in spite of the orientation invariant form of Eq. (18) the magnitude of this vector varies with the direction of the field. This is demonstrated in Fig. 1 but also is easily seen by keeping in Eq. (11) only one of the components of the field b_X, b_Y, or b_Z different zero, corresponding to the three limiting field directions along the three axes of the $\mathbf{U}$-frame.

In the case of pure isotropic hfi all diagonal elements of $\mathbf{G}_M$ matrix are equal to $Ma + v_{0I}$ and all off-diagonal elements are equal to zero giving an ENSF vector parallel to the field with magnitude $|\mathbf{v}_{I;M}| = |Ma + v_{0I}|$. If the hfi $\mathbf{A}$ and/or the $\mathbf{g}$-tensor are anisotropic, the field and the ENSF vector are no longer parallel. A limiting case of this situation is studied in detail in Appendix B.

4. General equations of the graphical method

One method to obtain enhanced visualization of the nuclear frequencies of ^{14}N, their orientation dependence, and the singularities in the powder spectra is associated with the graphical analysis of the Muha equation, Eq. (8). For this purpose, a new equation concerning the transition frequency between a pair of consecutive eigenvalues, can be derived from Eq. (8). This treatment follows exactly the mathematics in the isotropic case which was analyzed in detail elsewhere [8,9,11,12], but some quantities are more general, as it will be shown further. Thus, by substitution of the eigenfrequency λ' in Eq. (8), by the sum $\lambda + v$ to the value of λ of the next eigenvalue, and elimination the eigenfrequency λ for the transition frequency v gives the following relation:

$$q_M = \pm 3^{-3/2}(v^2 - p_M)(4p_M - v^2)^{1/2}. \tag{19}$$

Dividing both sides of the above Eq. (19) by $\tilde{v}_{I;M}^2$ and rearranging some terms the following equality is obtained:

$$F_M(|v_{I;M}|; v) = f_M(\mathbf{v}_{I;M}), \tag{20}$$

where

$$F_M(v; \vartheta, \varphi) = \frac{1}{\tilde{v}_{I;M}^2}\left\{2(1 - \eta^2) \pm 3^{-3/2}\right.$$
$$\times \left[v^2 - (\tilde{v}_{I;M}^2 + \eta^2 + 3)\right]$$
$$\left.\times \sqrt{4(\tilde{v}_{I;M}^2 + \eta^2 + 3) - v^2}\right\}, \tag{21}$$

$$f_M(\vartheta, \varphi) \equiv -\frac{1}{\tilde{v}_{I;M}^2}\left[\tilde{v}_{I;M}^2 - 3\tilde{v}_z^2 + \eta(\tilde{v}_y^2 - \tilde{v}_x^2)\right]$$
$$= -1 + \frac{3v_z^2 + \eta(v_x^2 - v_y^2)}{v_{I;M}^2}. \tag{22}$$

The dependence of F_M only on the magnitude of the reduced $|\tilde{v}_{I;M}| \equiv |v_{I;M}|/K$ and therefore also on the nqi, in contrast to the dependence of f_M on the not-normalized full $\mathbf{v}_{I;M}$ vector should be emphasized. This difference gives the possibility for the graphical method to be applicable as it is required by the method of the *separation of variables*. This principle is more straightforward in the isotropic hfi case where the function f depends of the field orientation while $|v_{I;M}|$ is constant [11].

The reduced eigenfrequencies of the nqi tensor appear as a product, $2(1 - \eta^2) = 2(1 - \eta)(1 + \eta)$, in the constant coefficient of the secular equation q_M. The second equality in the Eq. (22) for the function f_M emphasizes the complete independence of f_M on the strength of the nqi. This function is obviously bounded since $|\eta| < 1$ and the components of the vector $\mathbf{v}_{I;M}$ have to be shorter than its total length. In spite of this, the function f_M exhibits strong orientation dependence, and it is also depending on the sublevel $M = \pm 1/2$, see further.

Using the angles ϑ_M and φ_M which define the orientation of the ENSF vector $\mathbf{v}_{I;M}$ in the **U**-frame the function f_M in Eq. (22) can be rewritten in the following form:

$$f_M(\vartheta, \varphi; \Omega_g, \Omega_A) = -1 + 3\cos^2\vartheta_M + \eta\sin^2\vartheta_M$$
$$\times \cos 2\varphi_M. \tag{23}$$

This is the generalization of the function,

$$f(\vartheta, \varphi) = -1 + 3\cos^2\vartheta + \eta\sin^2\vartheta\cos 2\varphi. \tag{24}$$

which occurs in the isotropic hfi case. However, the limiting values of the function $f_M = -1 - \eta$ and 2 for $\mathbf{v}_{I;M}$ along the Y and the Z principal directions, respectively, are the same as in the isotropic case irrespective the magnitude of the hfi anisotropy and the nqi interaction.

The most straightforward way to check these characteristic values of f_M is to set the magnitude of the vector $\mathbf{v}_{I;M}$ in the Eq. (22) equal to the values v_Y and v_Z, respectively, and the other two components to zero. These extreme values correspond to the Y and the Z directions for the $\mathbf{v}_{I;M}$ oriented along $(\vartheta_M, \varphi_M) = (90, 90)$ and $(0, 0)$ degrees, respectively, for $\eta > 0$. According to Eq. (9) $\mathbf{v}_{I;M} = \mathbf{G}_M \cdot \mathbf{b}$ the external magnetic field $\mathbf{b}$ does not need in general to be directed along the principal axes of the **Q**-tensor when the $\mathbf{v}_{I;M}$ vector does. The matrix $\mathbf{G}_M$ acts as a transformation of the field which turns $\mathbf{v}_{I;M}$ away from the field direction $\mathbf{b}$, depending on the degree of the anisotropy. Furthermore, since $\mathbf{G}_M$ is not unitary the magnitude of the $\mathbf{v}_{I;M}$ vector will vary with the field orientation. (In the special case where the principal axes of **Q** and **A** tensors coincide the magnetic field and the ENSF vector remain parallel even in the anisotropic hfi case.)

Fig. 2 shows the function $F_M(v)$ calculated for different values of $\tilde{v}_{I,M}^2$ with fixed value of η. The function $F_M(v)$ consists of two branches, one for each of the signs $\pm$ in Eq. (21) and overlapping sets of definition $v \in [0, v_{\lim}]$, where

$$\tilde{v}_{\lim} = 2\sqrt{\tilde{v}_{I;M}^2 + \eta^2 + 3}. \tag{25}$$

The value of $v_{\lim}$ is fixed by the hfi and the magnitude of the external field in the isotropic case, but in the anisotropic case $v_{\lim}$ is fully determined only as soon as the field orientation also is known. Obviously, $v_{\lim}$ varies in a similar way as $|v_{I;M}|$ shown in Eqs. (11) and (12) and visualized by Fig. 1. Also, $v_{\lim}$ is the largest frequency for which F is defined and where the two branches of F meet exactly. For later use and for the sake of better orientation in the graphical solution one should note also that $F(v_{\lim}) = F(v_C) = 2(1 - \eta^2)/|v_{I;M}|^2$, where $v_C = v_{\lim}/2 = (p_M)^{1/2}$ is the middle point of the frequency interval $[0, v_{\lim}]$, where the function F_M is defined. Furthermore, F is symmetric with respect to reflection about the horizontal line $F_M(v_C) = F_M(v_{\lim})$, called further *the median* of F.

The graphical solution of the single crystal problem is represented by the intercepts of the functions $F_M(v)$ and f_M for each particular orientations of the field (ϑ, φ), corresponding to a certain orientation (ϑ_M, φ_M) of $\mathbf{v}_{I;M}$. The function $F_M(v)$ is first plotted vs. the transition frequency v for the direction (ϑ, φ) of the external field, while for that particular orientation the value of the function f_M is represented by a horizontal line in the same 2D-plot such as in Fig. 2. The transition frequencies v, where F crosses a horizontal f-line, correspond to the *single crystal* solutions of the *secular equation* for that particular *orientation of the field*. The two lower frequencies belong to the single-quantum (*sq*) transitions and third, the high frequency one, corresponds to the double-quantum (*dq*) transition.
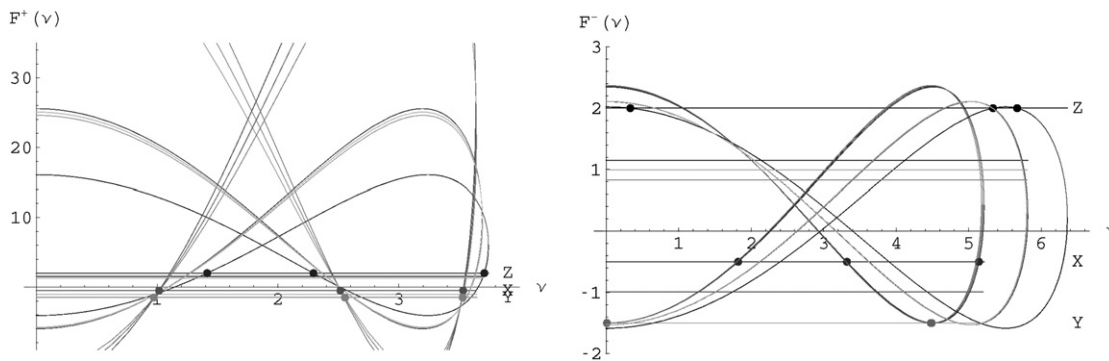
Fig. 2. Variation of the function $F(v)$ with the orientation of the field. The field went round in the first octant of the unit sphere in the following path of the spherical polar coordinates $(\vartheta, \varphi) = \{(1)\ Z(0, 0); (2)\ ZX(45, 0); (3)\ X(90, 0); (4)\ XY(90, 45); (5)\ Y(90, 90); (6)\ ZY(45, 90); (7)\ XYZ(45, 45)\}$. The orientations of the field along the three principal directions of the **Q**-tensor are particularly clarified in this figure by the heavy points of the $F = f$ intersections. Parameters: $a = 2.12$ MHz, $T = 0.5$ MHz, $\delta = 0.05 \Rightarrow \mathbf{A} = (1.645,\ 1.595,\ 3.12)$ MHz. $K = 1$ MHz, $\eta = 0.5 \Rightarrow \mathbf{Q} = (-0.5,\ -1.5,\ 2.0)$ MHz, and coincident tensors **A,Q**; $v_{0I} = -1.06$ MHz. The isotropic part of the hfi in the $M = 1/2$ manifold is cancelled exactly by the nuclear Zeeman, i.e., $M\,a + v_{0I} = 0$ MHz. Notice also that in all the F-plots the relation $F(v_{\lim}) > 2 \equiv f(Z)$ is valid for the cancelled manifold. For the non-cancelled manifold $M = -1/2$ the variation of the F-function with the orientation of the field leads to a great spread of the single quantum transitions and the value of the $v_{\lim}$.

Two special isotropic cases were widely used for the practical analysis of the spectra and the estimation of the hyperfine and quadrupole couplings. In one case the isotropic hyperfine coupling a exceeded significantly v_{0I} and K thus the $\tilde{v}_{I,M} > 1$ in both manifolds. In the second case, the hyperfine coupling $a/2 \cong v_{0I}$ gave $\tilde{v}_{I,M} \cong 0$ and $2v_{0I}$, respectively, in the two manifolds. The influence of the anisotropic hfi on the ESEEM and ENDOR spectra for these two important cases is specifically considered in this work.

5. Characteristic directions of the magnetic field

For the orientations of the ENSF vector along the directions X, Y, and Z, the magnetic field will confine itself along modified characteristic directions X', Y', and Z' under the influence of the anisotropy of the **A** tensor. It will be shown how the modified characteristic directions can be computed. An example is given by the determination of the characteristic direction Z'. For this purpose it is required that the ENSF vector $\mathbf{v}_{I,M}$ points along the Z-direction of the principal **U**-frame. Since the field direction under the above described conditions must be parallel to the new principal frame axis Z' which is unknown so far, the following equation can be written:

$$\mathbf{v}_{I;M} \equiv |v_Z(M)| \begin{pmatrix} 0 \\ 0 \\ 1 \end{pmatrix} = \mathbf{G}_M \cdot \mathbf{b}'. \tag{26}$$

It is easy to reverse this vector equation and solve for $\mathbf{b}'$, a task which within the present theoretical framework can be performed also analytically in principle using Eqs. (14)–(17).

$$\mathbf{b}' = |v_Z(M)| \mathbf{G}_M^{-1} \cdot \begin{pmatrix} 0 \\ 0 \\ 1 \end{pmatrix} = |v_Z(M)| \begin{pmatrix} [\mathbf{G}_M^{-1}]_{XZ} \\ [\mathbf{G}_M^{-1}]_{YZ} \\ [\mathbf{G}_M^{-1}]_{ZZ} \end{pmatrix}. \tag{27}$$

Since the $\mathbf{b}'$ is a unit vector one can simultaneously determine the magnitude of the ENSF vector using the following equation.

$$|v_Z(M)| = |v_{I,M}| = 1 \Big/ \sqrt{[\mathbf{G}_M^{-1}]_{XZ}^2 + [\mathbf{G}_M^{-1}]_{YZ}^2 + [\mathbf{G}_M^{-1}]_{ZZ}^2}. \tag{28}$$

The other two characteristic directions X', Y' of the field can be determined similarly, using the first and the second column of the inverted $\mathbf{G}_M$ matrix, respectively, considering the configurations for which $\mathbf{v}_{I;M}$ points along the X and Y directions. Notice that the only parameters included in the specification of the characteristic directions were the relative orientation of the **A** and the **Q** tensor (the Euler angles Ω_A). In the anisotropic case, the three modified characteristic directions of the field are in general not orthogonal. Examples of the calculation of the new characteristic direction for only **A**-tensor anisotropy are demonstrated in Appendix B and visualizations of the new directions are seen later together with the graphical solution. The parameters used in the calculations and the graphical method were the same as the ones in the full spectral simulation. In the graphical approach, the columns (vectors) of the inverses of $\mathbf{G}_\alpha$ and $\mathbf{G}_\beta$, representing the new characteristic directions for the two manifolds, are referred to the **Q**-tensor principal frame.

When the **g**-tensor is anisotropic the matrix $\mathbf{G}_M$ in Eq. (9) becomes also dependent on the field orientation through the variation of the effective **g**-factor $g'(\vartheta, \varphi)$ in Eq. (10), and the new characteristic directions cannot be determined by using the above simple method. For this

reason the **g**-tensor anisotropy will be treated in a separate work, where also a recursive variation of the above method will be exemplified.

6. Transition frequencies along the characteristic directions

It is not difficult even in the anisotropic case to obtain analytical expressions for the nuclear (ESEEM/ENDOR) *transition frequencies* when the magnetic field is along the *modified characteristic directions* due to the hfi and/or **g**-tensor anisotropy.

The following equations display those remarks:

$$\left.\begin{array}{l} dq : \tilde{v}_1^{(X)} = 2\sqrt{\tilde{v}_X^2 + \frac{(\eta+3)^2}{4}} \\ F : \tilde{v}_{2,3}^{(X)} = \frac{1}{2}\left|3(\eta-1) \mp 2\sqrt{\tilde{v}_X^2 + \frac{(\eta+3)^2}{4}}\right| \end{array}\right\} \quad (29a)$$

for $v_{I;M}\|\mathbf{X}$ and $\mathbf{B}_0\|\mathbf{X}'$,

$$\left.\begin{array}{l} F : \tilde{v}_{1,3}^{(Y)} = \frac{1}{2}\left|3(\eta+1) \pm 2\sqrt{\tilde{v}_Y^2 + \frac{(\eta-3)^2}{4}}\right| \\ dq : \tilde{v}_2^{(Y)} = 2\sqrt{\tilde{v}_Y^2 + \frac{(\eta-3)^2}{4}} \end{array}\right\} \quad (29b)$$

for $v_{I;M}\|\mathbf{Y}$ and $\mathbf{B}_0\|\mathbf{Y}'$,

$$\left.\begin{array}{l} F : \tilde{v}_{1,2}^{(Z)} = \left|3 \pm \sqrt{\tilde{v}_Z^2 + \eta^2}\right| \\ dq : \tilde{v}_3^{(Z)} = 2\sqrt{\tilde{v}_Z^2 + \eta^2} \end{array}\right\} \quad \text{for } v_{I;M}\|\mathbf{Z} \text{ and } \mathbf{B}_0\|\mathbf{Z}'. \tag{29c}$$

The *characteristic transition frequencies* are given in reduced K units of the quadrupole strength in order to

achieve compact notations. Explicit expressions for the reduced components of the ENSF vector $\tilde{v}_{I;M} = (\tilde{v}_{I;M}^{(X)}, \tilde{v}_{I;M}^{(Y)}, \tilde{v}_{I;M}^{(Z)}) \equiv (\tilde{v}_X, \tilde{v}_Y, \tilde{v}_Z)$ which appear under the square roots were derived in an earlier section, Eqs. (9) and (14–17), valid for anisotropic hfi but isotropic **g**-tensor. Analytical computations for some limiting cases are considered in detail in Appendix B. The M-dependence of the above transition frequencies should also be pointed out. They were computed as differences of the frequency eigenvalues of the simplified secular equations which come about by considering the field along each one of the three characteristic directions. Suppose that the field is chosen along X characteristic direction. The corresponding pure quadrupole state $|X\rangle$ remains unscrambled in both manifolds and does not contribute to the ESEEM spectrum as it will be explained further. The other two pure quadrupole states $|Y\rangle$ and $|Z\rangle$ mix by the effective nuclear Zeeman. The ESEEM transition appears at the difference of their eigenfrequencies,

$$v^X = |\lambda_Y - \lambda_Z|; \text{(cyclic)}. \tag{30}$$

Only two ESEEM transitions can be observed in this case, the transitions $v_1^{(X)}(M = \pm1/2)$ in the two sublevels. The remaining ESEEM transitions $|X\rangle \leftrightarrow |Y\rangle$ and $|X\rangle \leftrightarrow |Z\rangle$ which involve the pure quadrupole state $|X\rangle$ cannot be observed because no *branching* of these states through any other is impossible. The two identical states can be formally labeled by the sublevel- projection $S_{z'} \equiv M = \pm1/2$, i.e., $|X_M\rangle$, and must be considered *sublevel-M degenerate*. A simplified variation of the graphical method in the Fig. 3, treating rather the *eigenfrequencies* than the *transition frequencies*, is best demonstrating some of these facts.

Actually any of the Eqs. (29) gives back the *pure quadruple* frequencies for conditions of *full cancellation*
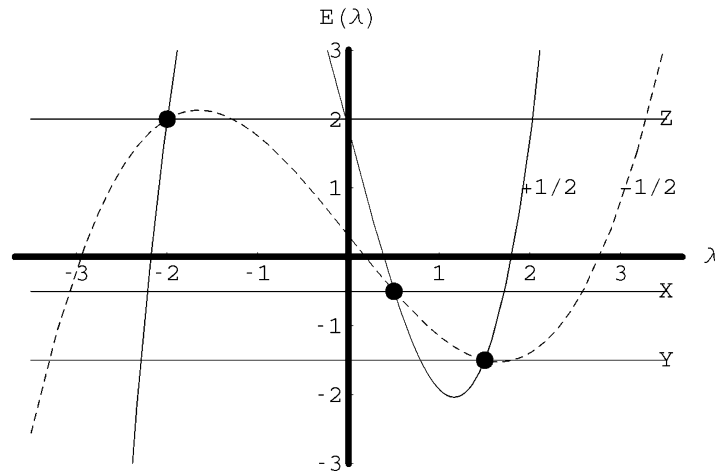

Fig. 3. Plot of the eigenfrequencies function $E(\lambda) = [\lambda^3 - p_M\lambda + 2(1 - \eta^2)]/\tilde{v}_{I;M}^2$ along with the horizontal lines for the characteristic values of the *f*-function $f(\vartheta, \varphi)$, revealing the manifold M-degeneracy of the pure quadrupole eigenstates $|X\rangle$, $|Y\rangle$, and $|Z\rangle$ with eigenvalues $1 + \eta$, $-1 - \eta$, and 2, respectively, occurring for the characteristic directions of the field. The nqi constant and the asymmetry parameter were $K = 1.6$ MHz and $\eta = 0.5$, respectively, while the isotropic case with scalar hf-coupling constant $a = 5$ MHz and $v_{0I} = -1.06$ MHz was taken for the purpose of easier demonstration of this method.

$v_{I;M} = 0$. The relations in Eq. (29) however are not limited to cancellation but they are quite general regarding the magnitude of the frequency $\mathbf{v}_{I;M}$. They do not either require isotropic hfi/$\mathbf{g}$-tensors. Analogous expressions have been given in the Table 1 of the article of Lee et al. [12] for the case of all three $\mathbf{g}$, $\mathbf{A}$, and $\mathbf{Q}$ tensors coinciding, while the above relations include even non-coinciding tensors through the square of the components v_X, v_Y, and v_Z for arbitrary ENSF vector. However, Lee et al. refer to transitions under orientation selection conditions and they denote these limiting solutions according to Muha, so that comparison to the solutions $v_1^{(X)}$, $v_2^{(Y)}$, and $v_3^{(Z)}$ of the present work is not easy. It was verified however that the analytical transition frequencies in both works were identical for conditions where both were valid.

In the limit of small effective nuclear Zeeman frequencies $v_{I;M}$, i.e., for very low field and hfi or under cancellation conditions of the isotropic part of the hfi, the above three solutions become approximately equal to the pure quadrupole frequencies, $(3 \pm \eta)K$, $2\eta K$. They correspond to X-, Y-, and Z-polarized transitions, or to the more used symbols v_+, v_-, and v_0, of Flanagan and Singel [11]. To the other extreme of large effective nuclear Zeeman the explicit solutions $v_1^{(X)}$, $v_2^{(Y)}$, and $v_3^{(Z)}$ become high-frequency $\boldsymbol{dq}$ transitions.

Summarizing this section, only the transitions at the frequencies $v_1^{(X)}$, $v_2^{(Y)}$, and $v_3^{(Z)}$ in Eq. (29) will be visible in *single crystal* ESEEM spectra. These are the transitions that do not involve the corresponding manifold-degenerate states $|X_M\rangle$, $|Y_M\rangle$, and $|Z_M\rangle$, respectively, for $M = \pm 1/2$. However, even the other two (Forbidden) transition frequencies $v_{2,3}^{(X)}$, $v_{3,1}^{(Y)}$, and $v_{1,2}^{(Z)}$ for each characteristic orientation are important for powders because they represent the *stationary points* of the transition frequency v with respect to corresponding field orientations. The *ideal* ENDOR *powder spectra*, Ref. [17], are expected to obtain the characteristic patterns at all the frequencies of Eq. (29).

7. Stationary points

The appearance of the characteristic features in the powder spectra is connected with stationary points of the transition frequency $v(\vartheta, \varphi)$ at the field orientation (ϑ, φ), which can be determined from the graphical intersections of the functions F_M and f_M and the manipulation of the matrix $\mathbf{G}_M$.

The particular shape of the *characteristic features*, such as *divergences maxima* or *steps* depends mainly on the kind of the stationary point, which can be a maximum, a minimum, or a saddle point! Furthermore, the characteristic shapes vary if the location of the extremum is on the **rand** (at the limiting points of the set of definition) of the function $v(\vartheta, \varphi)$ or at a point inside the definition set.

A useful equation for the stationary points of the transition frequencies $v(\vartheta, \varphi)$, which connects directly the differentials of f and v, decreasing thus the formal dimensions of the problem to two, can be derived.

$$dv = df / F'(v). \tag{31}$$

A similar equation was given first for the CW-EPR resonant fields by Kottis and Lefebvre [10]. This relation shows that there exist two different kinds of stationary points of interest in the present context. One of them can be obtained for finite derivative $F'(v)$ for $df = 0$, and the second when the derivative $F'(v)$ diverges to infinity. Both cases are important for the ENDOR/ESEEM powder lineshapes.

The first kind of stationary points is easiest exemplified for coinciding tensors. The transition frequencies can be read directly on the frequency axis at the crossings of the F with the horizontal lines f when the field is along the principal axes of the $\mathbf{Q}$-tensor. For non-coincident tensors the *modified* characteristic directions X', Y', and Z' of the field must be determined before a graphical solution is possible.

From the diagrammatic solutions in the present paper, it can be observed that in most cases F satisfies the condition $F' \neq 0$ at a stationary point. However, there are exceptions where the f lines are very close to a horizontal tangent of the F curve. This can happen in two cases: (i) if the values of two solutions are very close, (ii) for the lowest-frequency intersections $F \cap f$ in systems with relatively large $\mathbf{v}_{I;M}$. (These cases are visualized in the $Y(-)$ intersection of the later Fig. 7(p) The corresponding ESEEM transition frequencies usually are not visible.

The $df = 0$ case concerns primarily the *sq* transitions which are generally difficult to observe in the anisotropic $\mathbf{g}/\mathbf{A}$ case because they require small $\mathbf{v}_{I;M}$, i.e., a great deal of cancellation of the nuclear Zeeman by the hfi, while full cancellation is a rare event in the anisotropic case.

A high-frequency transition assigned as a *limiting* $\boldsymbol{dq}$ transition is approximately equal to the $v_{\lim}$ and can be influenced also by the second kind of characteristic points discussed next and may result to a step down to zero intensity. Since the derivative F' becomes infinite for $v = v_{\lim}$, the particular field orientations (ϑ, φ) could lead to accumulation of transitions in a small frequency interval, and great intensity around this point in powders, in spite of eventually small transition probabilities [10]. Among the possible characteristic powder patterns, a *maximum* is expected for this point followed by a *step* down to zero intensity. This is the only *stationary v point* not related to a single *characteristic direction* and is thus unimportant for single crystal spectra. The corresponding patterns of the powders will generally occur at high frequency, higher than the extreme intercepts with the f function affecting the broadening of the $\boldsymbol{dq}$ transitions.

There are some additional factors that contribute to the actual shape of the characteristic features in orienta-

tion-disordered ESEEM spectra in comparison with ENDOR. The *characteristic features* described above exist always for ideal ENDOR powders [17] but additional effort is required to find the modified features in ESEEM powders due to the vanishing intensities imposed by the selections rules of ESE experiment at just the characteristic directions. These general considerations are illustrated in details in the following sections.

8. Influence of the anisotropic hfi on the double-quantum peaks

In the anisotropic case, the turning point $v_{\lim}$ of the function F is different for each orientation of the field and can be determined by Eq. (25). Its position has not a direct connection to the solution of the secular equation in single crystals except for the rare case for which $v = v_{\lim}$ is a valid ESEEM/ENDOR transition frequency. In powders, the maximum of the frequency $v_{\lim}$ can be a stationary point of the function $v(\vartheta, \varphi)$. As the $v_{\lim}$ varies with $\mathbf{v}_{I;M}$ according to Eq. (25), see Fig. 1, it becomes important to consider the spread of the frequency $v_{\lim}$ in the transition-frequency axis.

Thus, the $v_{\lim}$ feature does not contribute always to the powder spectra, or at least it is not a distinct additional solution. One clear case is the exact cancellation for isotropic hfi, in which the cancelled manifold contributes to the powder lineshape by three sharp pure quadrupole peaks. Bringing up the analogy to systems with small hf anisotropy ($T/a_{\mathrm{iso}} < 0.2$) and cancellation of the isotropic part one can agree that the relation $2 < 2(1 - \eta^2)/\tilde{v}_{I;M}^2$ or equivalently the strong quadrupole condition $|v_{I;M}| < |K|(1 - \eta^2)$ will lead to three relatively sharp, nearly pure quadrupole peaks. This inequality strongly depends on the relative values of η^2 and $\tilde{v}_{I;M}^2$. The median of F at the height $F_M(v_{\lim})$ in this case lies much higher than the $F_M = f_M$ intersections for the cancelled manifold with for $M = 1/2$ as seen in the Fig. 8. The frequencies of the corresponding peaks are organized in three groups of similar frequencies with the high-frequency peaks being slightly smaller than $v_{\lim}$.

Let the $v_{\lim}$ correspond to the orientations (ϑ_M, φ_M) of the ENSF vector satisfying the condition:

$$\varepsilon_M = -1 + 3\cos^2\vartheta_M + \eta\sin^2\vartheta_M \cos 2\varphi_M, \tag{32}$$

which leads to,

$$\cos^2\vartheta_M = 1 - \frac{2 - \varepsilon_M}{3 - \eta \cos 2\varphi_M} \tag{33}$$

with $0 \leqslant \varepsilon_M = 2(1 - \eta^2)/\tilde{v}_{I;M}^2 \leqslant 2$ when the cosine of ϑ_M is defined.

According to the above definitions, ε_M signifies the particular value of f_M for which the ENSF vector $\mathbf{v}_{I;M}$ has a particular orientation giving the transition frequency $v_{\lim}$.

In the case of isotropic hfi where ε_M is constant for each manifold, the connected set of orientations (ϑ_M, φ_M) satisfying the condition in Eq. (33) contributes to the intensity of the $v_{\lim}$ peaks appearing at the frequencies,

$$v_{\lim,\pm} = 2\sqrt{(v_{0I} \pm a/2)^2 + K^2(3 + \eta^2)}. \tag{34}$$

For the anisotropic case, it is clear that the orientations corresponding to $v_{\lim}$ generally differ from the characteristic directions **U**, the principal axes of the nqi tensor. For instance $\cos^2\vartheta_M = 1$ is obtained for $\varepsilon_M = 2$ that strictly requires $1 - \eta_2 = \tilde{v}_{I;M}^2$, a condition not fulfilled for an arbitrary system (see Appendix C), while $\cos^2\vartheta_M = 0$ is also fulfilled in another particular situation with $\eta = 1$ at $\varphi_M = 0$. The value of ε_M depends on the orientation of the ENSF vector and $v_{\lim}$ varies between $(v_{\lim})_{\min}$ and $(v_{\lim})_{\max}$, which are determined by $(v_{I;M}^2)_{\min}$ and $(v_{I;M}^2)_{\max}$, respectively. Because the $v_{I;M}^2$ computation can be performed in any coordinate system, it is easy to find the minimum and maximum values of $v_{I;M}^2$ in the principal frame of the hyperfine tensor. In the simple case of the axial hfi,

$$v_{I;M}^2 = v_{\perp,M}^2 + (v_{\parallel,M}^2 - v_{\perp,M}^2)\cos^2\vartheta_B, \tag{35}$$

where ϑ_B stands for the orientation of the magnetic field relative to the unique axis of the hf tensor and,

$$v_{\perp,\pm} = v_{0I} \pm \frac{a - T}{2}; \quad v_{\parallel,\pm} = v_{0I} \pm \frac{a + 2T}{2}. \tag{36}$$

The expression in Eq. (35) shows that $(v_{I;M}^2)_{\min}$ is equal to the smaller of the components $v_{\perp,\pm}^2$ or $v_{\parallel,\pm}^2$, while $(v_{I;M}^2)_{\max}$ is equal to the larger of them, if the condition $0 \leqslant \varepsilon \leqslant 2$ is fulfilled for all orientations of the magnetic field. This condition guarantees that the wished transition frequency $v = v_{\lim}$ is included among the set of the solutions of the secular equation for some of the orientations of the field.

9. Analytical applications

Fig. 4A shows the (stimulated) three-pulse ESEEM and ideal ENDOR spectra [17] calculated with $a = 5$ MHz, $K = 0.4$ MHz, $\eta = 0.5$, and $|v_{0I}| = 1.06$ MHz, in the absence of the anisotropic hfi, and for axial anisotropic tensor with perpendicular components $T = \pm 0.5$ MHz for coincident axes of the nqi and hfi tensors. Fig. 4B shows spectral simulations of ESEEM and ENDOR with the same parameters as above but for misalignment $\beta = 60°$ between the Z axes of the **Q**- and **A**-tensors.

Only two peaks dominate the ESEEM spectrum for $T = 0$. Their frequencies at 7.24 and 3.22 MHz almost exactly correspond to the frequencies (7.26, 3.22) MHz predicted by Eq. (34). The sharpest ENDOR peaks occur at the same frequencies.

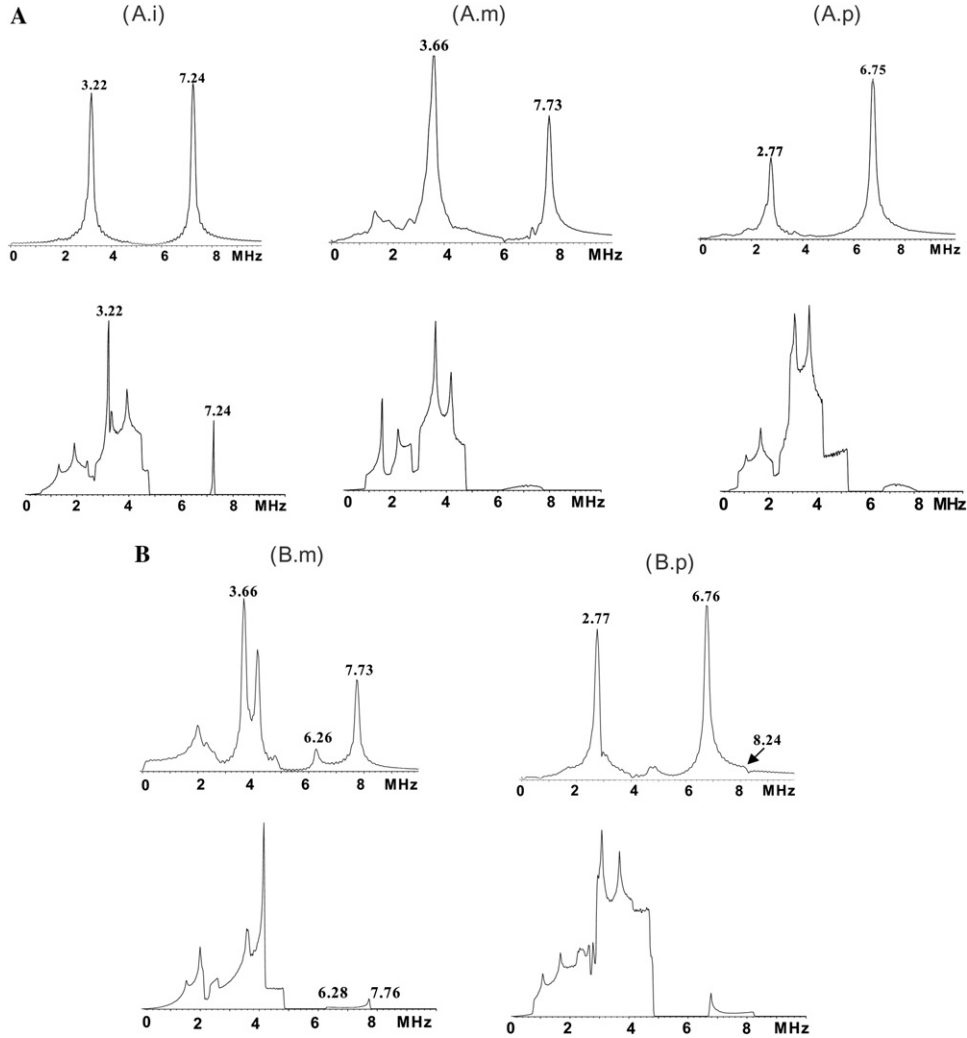The introduction of the anisotropic hfi with two opposite values of $T = \pm 0.5$ MHz, shifts the frequencies

Fig. 4. (A) Simulations of *stimulated* ESEEM spectra ($\tau = 200$ ns), higher panels, *ideal* ENDOR [17], lower panels, for the following parameters: $K = 0.4$ MHz and $\eta = 0.5$, or $\mathbf{Q} = (-0.20, -0.60, 0.80)$ MHz; $|v_{0I}| = 1.06$ MHz, and $a = 5$ MHz, and coinciding nqi and hfi tensors. The traceless part $\mathbf{T}$ of the hfi-tensor is defined as $(-T, -T, 2T)$. (i) $T = 0$; (m) $T = -0.5$ or $\mathbf{A} = (5.5, 5.5, 4.0)$ MHz; (p) $T = 0.5$ or $\mathbf{A} = (4.5, 4.5, 6.0)$ MHz. In the isotropic case we have: ESEEM peaks: 7.24, 3.22 MHz. ENDOR peaks and steps: 7.24, 4.76, 4.5, 3.92, 3.3, 3.22, 2.38, 1.9, 1.3, and 0.64 MHz. (B) ESEEM and ENDOR simulations with the same parameters as in (A) but for non-coinciding $\mathbf{A}$ and $\mathbf{Q}$-tensors. (m) $T = -0.5$ MHz, (p) $T = 0.5$ MHz. Relative orientation of nqi and hfi tensors: $(0, 60°, 0)$.

of both major peaks to opposite directions, i.e., to higher frequencies for $T = -0.5$ MHz and to lower frequencies for $T = 0.5$ MHz. This is easily seen in the following equations, which depict the *characteristic dq* transition frequencies in the case of coincident principal directions of the nqi and hfi tensors. They were given earlier in this text by Eq. (29) and were adapted for the present axial hfi case, see Appendix B.

$$v_{X;\pm}^{dq} = 2\sqrt{[v_{0I} \pm (a - T)/2]^2 + K^2(3 + \eta)^2/4}, \tag{37a}$$

$$v_{Y;\pm}^{dq} = 2\sqrt{[v_{0I} \pm (a - T)/2]^2 + K^2(3 - \eta)^2/4}, \tag{37b}$$

$$v_{Z;\pm}^{dq} = 2\sqrt{[v_{0I} \pm (a + 2T)/2]^2 + K^2\eta^2}. \tag{37c}$$

For instance, for $T = 0.5$ MHz the following pairs of values were obtained in the two manifolds $M = \pm 1/2$: $(v_X, v_Y)_{dq;+} = (6.77, 6.69)$ MHz and $(v_X, v_Y)_{dq;-} = (2.76, 2.58)$ MHz. They are actually very close to the values (6.75, 2.77) MHz of the simulated spectra in Fig. 4A(m) and also to the $v_{\lim}$ values (6.77, 2.78) MHz computed by the following equation, which assumes orientation of the magnetic field in XY plane.

$$(v_{\lim})_{\perp;\pm} = 2\sqrt{[v_{0I} \pm (a - T)/2]^2 + K^2(3 + \eta^2)}. \tag{38}$$

However, it is certain that the latter frequencies in Eq. (38) cannot contribute to the spectrum, because the characteristic directions of the field and the direction the $v_{\lim}$ differ in general according to the above discussion and Appendix C. Thus, one can conclude that in

the presence of axial hyperfine coupling the *characteristic dq* peaks which appear in the ESEEM/ENDOR spectra correspond to the orientations of the magnetic field in the XY-plane of the hyperfine tensor. This is supported by the shape of the simulated low-frequency *dq* line, which has a shoulder at 2.56 MHz in the calculated ESEEM spectrum, corresponding to the above peak with frequency $(v_Y)_{dq;-} = 2.58$ MHz.

Similar conclusion can be made for the ESEEM spectrum calculated with $T = -0.5$ MHz.

The ESEEM spectra calculated for non-coincident axes of nqi and hfi tensors (Fig. 4B), in addition to the maxima close to $(v_{dq})_{X,M}$ or $(v_{lim})_{\perp,M}$ show two smaller features at 6.26 and 8.24 MHz for $T = -0.5$ and 0.5 MHz, respectively, both arising from the same $M = 1/2$ manifold. Their positions are well-described by the equation for v_{lim} for the orientation of the magnetic field parallel to Z axis,

$$(v_{lim})_{\parallel;\pm} = 2\sqrt{[v_{0I} \pm (a + 2T)/2]^2 + K^2(3 + \eta^2)}, \qquad (39)$$

which gives calculated frequencies 6.29 and 8.24 MHz. They exceed the *characteristic dq* frequencies for this orientation, which are 6.13 and 8.13 MHz, computed by Eq. (37c) for $(v_{dq})_{Z;\pm}$.

These observations suggest that for non-coincident axes the frequencies $(v_{lim})_{max,M}$ and $(v_{lim})_{min,M}$ correspond to some intermediate orientation of the ENSF vector and thus can contribute to the spectrum. The frequencies $(v_{lim})_{\parallel,M}$ for the opposite manifolds were computed to 2.37 and 4.14 MHz but were not present in the ESEEM spectra. However, observation of the $(v_{lim})_{\parallel,M}$ even from one manifold opens the way for the determination of $A_{\parallel} = a + 2T$. Knowledge of $A_{\perp}$ and $A_{\parallel}$ allows the determination of a and T values separately. It is important that the positions of the *limiting dq* maxima in ESEEM spectra do not depend on the angles describing the relative orientation of the nqi and hfi tensors and can be used for the direct determination of the $A_{\perp} = a - T$ and $A_{\parallel} = a + 2T$.

In the simulated ENDOR spectra the appearance of spectral features at $(v_{lim})_{\perp,M}$ and $(v_{lim})_{\parallel,M}$ frequencies depended on the relative orientation of the nqi and hfi tensors. The ENDOR spectra did not show any maxima at the $(v_{lim})_{\perp,M}$ and $(v_{lim})_{\parallel,M}$ frequencies for coincident axes of the nqi and hfi tensors. The intensity was suppressed at these frequencies and a broad *dq* line without well-pronounced maximum was present in the spectra. However, for non-coincident axes the *dq* transition had the typical ENDOR "powder" lineshape with a maximum at $(v_{lim})_{\perp,M}$ and a step at $(v_{lim})_{\parallel,M}$. Similar behavior has been observed for other relative orientation of the nqi and hfi tensor.

Attempting to understand the above observations, it was shown (Appendix C) that for these orientations for which the v_{lim} is a solution of the secular equation,

the locus of the tip of the $\mathbf{v}_{I,M}$ vector must identify with the 3D surface of the following *hyperboloid of two sheets*, which circumvent the Z-axis.

$$\frac{\tilde{v}_Z^2}{(1 - \eta^2)} - \frac{\tilde{v}_X^2}{2(1 + \eta)} - \frac{\tilde{v}_Y^2}{2(1 - \eta)} = 1. \qquad (40)$$

Inspecting this surface it becomes clear that the $\mathbf{v}_{I,M}$ vector is prohibited to attain orientations parallel to the XY-plane of the $\mathbf{U}$-frame. Consequently, the intensity of the solutions $v = v_{lim}$ is minimized. On the other hand, for non-coinciding tensors the characteristic directions are not parallel to the $\mathbf{U}$-frame anymore and the possibility of the transition $v = v_{lim}$ for the ENSF vector nearly parallel to a *modified characteristic direction* are significantly increased, enhancing the transitions in question.

Looking a little closer the ENDOR spectra in Fig. 4B, it becomes clear that for misaligned **A**- and **Q**-principal axes both the high-frequency transitions $v_{lim,\perp}$ and $v_{lim,\parallel}$ are present. Furthermore, their relative intensity agrees with the typical spatial weight giving a peak for the perpendicular direction and a step for the parallel direction. Their intensity relative to the other peaks in the ENDOR spectra is comparatively small, but the absence of any other peaks in the high-frequency region of the present spectra makes their presence very clear. They are both features of the $M = 1/2$ manifold in agreement the high-frequency property and a formally positive nuclear resonance frequency $|v_{0I}|$. Furthermore, in the ESEEM spectra, these peaks are strongly amplified comparing to the powder ENDOR, the perpendicular edge being significantly more amplified against the parallel, which obtains the appearance of a weaker peak. For coinciding tensors the parallel peaks are completely absent in accord with the above discussion.

10. Comparison to the graphical method

Turning to the application of an *extended graphical approach* on the anisotropic case, it is noticed that the intersections of F for each of the characteristic directions and the corresponding f were correlated with the spectral features in the ENDOR or the ESEEM simulation, or both.

The simulated ESEEM peaks at 7.24 and 3.22 MHz for the isotropic hf case in Fig. 4A(i) corresponded almost exactly to the graphical solutions *dq*(−) 7.26 MHz and *dq*(+) 3.22 MHz obtained by conventional $F = f$ plots (not be shown) as in earlier studies.

Turning to the axial anisotropy case, the ESEEM/ENDOR simulations for $T = -0.5$ MHz in Fig. 4A(m) will be compared to the graphical intersections of Fig. 5(m). For greatest convenience of the reader the comparison between the ESEEM/ENDOR simulations with the graphical method will be performed using primitive
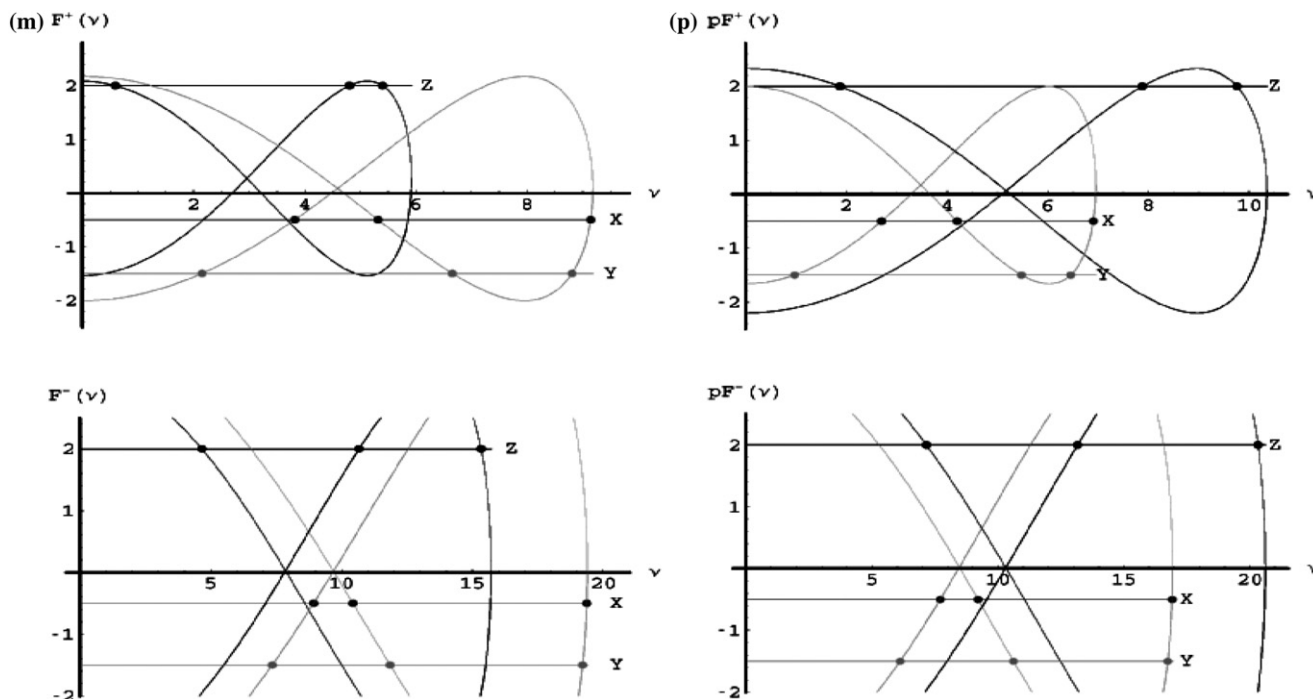
Fig. 5. The graphical solution for axial hfi for the axial cases of the same system as in Fig. 4A. The intersections of the *F* curve with *f* for the field along the principal **Q**-directions which are highlighted by the heavy points agree best to the simulations. (*v*-axis in reduced *K*-units. The figures in the following primitive diagrams are in MHz).

(m) $T = -0.5$ MHz.

```
ESEEM-----------1.54--2.075----2.77----3.66--------------------------------------------------7.12----7.73-
ENDOR-0.86--1.52------2.14---2.62----3.58----4.18---4.7-------------------6.2----------------7.74-
X(+)---------------1.53---2.13----------------3.66---------------------------------------------------
Y(+)-----0.86-----------------------2.66--3.53------------------------------------------------------
Z(+)--0.24------------1.99-2.16----------------------------------------------------------------------
X(−)-------------------------------------------3.57--4.17-----------------------------------7.75--
Y(−)---------------------------------2.94-------------------4.74---------------------------------7.69--
Z(−)-------------------1.87----------------------------4.27-------------------6.13---------------------
```

 (p) $T = 0.5$ MHz.

```
ESEEM---0.94----------1.87------2.56--2.77-----------3.66-------------------------6.75----------
ENDOR-0.76--1.08--1.68-----2.48--------2.9---3.08--3.68---4.72--5.24---------6.7---8.12----
X(+)--------------1.08--1.68---------------2.76-----------------------------------------------------
Y(+)--0.39------------------2.19---2.58-------------------------------------------------------------
Z(+)-----0.75------------------------------------3.15----3.90----------------------------------------
X(−)-------------------------------------------3.08--3.68-------------------------6.77----------
Y(−)--------------------------2.45----------------------------4.25------------------6.70-------------
Z(−)-------------------------------------------2.86-------------------------5.26-------------8.13----
```

diagrams. They are placed in the legend of the graphical method and display approximately the relative transition frequencies for each method from zero to the max frequency along consecutive text lines. The hits of the graphical intersection differing by less than 0.1 MHz are in bold.

The strongest *dq* peaks in the ESEEM simulation at 7.73 and 3.66 MHz appear also in the perpendicular *dq* intersections $X(-)$ 7.75 MHz and $X(+)$ 3.66 MHz, respectively. Among the weaker ESEEM peaks the

strongest at 1.54 MHz is found as $X(+)$ 1.53 MHz. The ESEEM at 7.73 MHz finds correspondence to the $X(-)$ 7.75 MHz, while the ESEEM peak at 2.075 MHz finds a graphical correspondence to the $X(+)$ intersection at 2.13 MHz, which agrees better with the ENDOR peak at 2.14 MHz. The ESEEM peak at 2.77 MHz finds no better correspondence than the $Y(+)$ at 2.66 MHz. On the other hand, the ENDOR peaks and steps at 0.86, 3.58, 4.18, 4.7, and 6.2 MHz find good correspondence to the graphical intersections $Y(+)$ 0.86,

3.53 MHz, $X(-)$ 4.17 MHz, $Y(-)$ 4.74 MHz, and $Z(-)$ 6.13 MHz, respectively.

The agreement of the ESEEM/ENDOR peaks in Fig. 4A(p) for $T = 0.5$ and the graphical intersections of Fig. 5(p), is also very good as seen in the primitive diagram.

The strongest *dq* peaks in the ESEEM simulation at 6.75 and 2.77 MHz appear also in the perpendicular *dq* intersections $X(-)$ 6.77 MHz and $X(+)$ 2.76 MHz, respectively. Among the weaker ESEEM peaks the one at 3.66 MHz is found as $X(-)$ 3.68 MHz, the 2.56 MHz as *dq* $Y(+)$ 2.58 MHz, while for the ESEEM peak at 1.87 MHz the closest graphical intersection $X(+)$ 1.68 MHz agrees exactly with the corresponding ENDOR peak at 1.68 MHz. Considering the ESEEM peak at the lowest frequency of 0.94 MHz the correspondence is best again between the closest ENDOR and the graphical solution at $X(+)$, both exactly 1.08 MHz. Finally the ENDOR peaks at 2.9, 5.24, and 8.12 find correspondence to the $Z(-)$ intersections at 2.86, 5.26, and 8.13, respectively.

For tilted tensors three different *F*-curves are necessary. In Fig. 6, the graphical solution for tilted **A**-, **Q**-principal frames is shown. The summary of the intersections together with the peaks and the steps of the simulations in Fig. 4B(m) ($T = -0.5$ MHz) appear in the legend of Fig. 6(m) for easy comparison.

In addition to the diagrammatic solutions, using Eqs. (38) and (39), two perpendicular and parallel $(v_{\lim})_{\max}$ doublets are expected for $|v_{0I}| = 1.06$ MHz, at about $dq_{\perp,\pm} = (7.76, 3.67)$ MHz and $dq_{\parallel,\pm} = (6.29, 2.37)$ MHz for $T = -0.5$ MHz. They were also introduced in the diagram in bold and italics in order to obtain a complete picture. The two perpendicular limiting bi dq peaks find correspondence to the strongest simulated ESEEM

peaks at 7.73 and 3.66 MHz. The corresponding ENDOR peaks agree also well. Even the parallel peaks at 6.29 MHz and at 2.37 MHz are in agreement with the relatively strong ESEEM peak at 6.26 MHz and the much weaker at 2.3 MHz. Among the fourth and fifth stronger ESEEM peaks at 4.15 MHz and at 2.00 MHz the first does not correspond to any graphical intersection while the closest *characteristic frequency* of the second is found at the intersections $Z_{\mathrm{ACT}}(-)$ 2.2 MHz. Among the weaker peaks the ENDOR transition at 1.52 is found exactly at the intersection $Z_{\mathrm{ACT}}(-)$ 1.52 MHz and the ESEEM/ENDOR at 4.8/4.82 MHz at $Z_{\mathrm{ACT}}(-)$ 4.88 MHz. The ESEEM/ENDOR peaks at 2.6 MHz is found at the intersection $Y_{\mathrm{ACT}}(+)$ 2.6 MHz.

Finally, the data from the ESEEM/ENDOR simulation for $T = 0.5$ MHz in Fig. 4B(p) and the graphical intersections at the modified characteristic directions in Fig. 6(p) are compared. The perpendicular $(v_{\lim})_{\max}$ doublet is expected according Eq. (38) for $|v_{0I}| = 1.06$ MHz at about $dq_{\perp,\pm} = (6.78, 2.78)$ MHz. The corresponding simulated ESEEM peaks at 6.76 and 2.77 MHz agree very well. Except for the above perpendicular limiting *dq* peaks the related parallel peaks $dq_{\parallel,\pm} = (8.25, 4.14)$ MHz were also computed using Eq. (39), and they were found to correspond to the simulated ESEEM and ENDOR peaks at 8.24 MHz and an ENDOR peak at 4.12 MHz, respectively. The last transition was not present in ESEEM in spite the heavy superposition in the band 3.68–4.8 MHz in the ENDOR simulation most probably the particular transition moments of ESEEM lead to very small relative intensities of the peaks in that interval. In the same interval, out of the two ESEEM transitions at 4.72 and 4.88 MHz present in the simulation, only the first is found in the graphical intersection as

Fig. 6. The graphical solution for axial hfi for the same system as in Fig. 4B, but tilted **A**, **Q** principal axes by $\beta = 60°$. Only the intersections of the *F* curves with the horizontal lines $f(X_{\mathrm{ACT}})$, $f(Y_{\mathrm{ACT}})$ and $f(Z_{\mathrm{ACT}})$ for which the field is along the modified characteristic directions count as solutions. The *limiting dq* transitions have to be computed separately, vide infra, and are seen in bold and italics. (*v*-axis in reduced *K*-units. The figures in the following primitive diagrams are in MHz).

(m) $T = 0.5$ MHz.

```
ESEEM---------------------2.0--2.3----2.6--------3.66--------4.15---4.8----------6.26------------7.73--
ENDOR------------1.52---2.00---------2.6-------3.6--3.84---4.16---4.82---------6.28------------7.76-
X_ACT(+)-----------------------------------2.96---3.6-----------------------------------6.52----------
Y_ACT(+)----0.84-------------------------2.6----3.52----------------------------------------------7.76-
Z_ACT(+)-0.16----------------------------2.6------------------------------6.29------------------
X_ACT(-)-----0.88---1.52------------2.44------------3.67---------------------------------------
Y_ACT(-)----------------------------2.88----------------------4.68----------------------------7.6-----
Z_ACT(-)---------------------2.2--2.37------------------------------------4.88----------------7.16---------
```

(p) $T = -0.5$ MHz.

```
ESEEM---------------------1.7----------2.77----------------------------------4.72----4.88--6.76----8.24-
ENDOR---0.76--1.08---1.68------2.66-2.78-2.92-3.08--3.68-4.12------4.7-----4.8----6.74-----8.24-
X_ACT(+)--------------1.44----2.08-------------------------3.56----------------------------6.78----------
Y_ACT(+)--0.48----------------2.08--2.6----------------------------------------------------------------
Z_ACT(+)-0.12----------------------2.44---------------------------------------------------------------8.25
X_ACT(-)--------------------------------2.78-------------3.56---4.24----------------------7.72--------
Y_ACT(-)----------------------------2.36----------------------------4.24----------------6.56-------------
Z_ACT(-)----------------------------2.08--------------------------- 4.14------4.72--------------6.84-------
```

$Z_{ACT}(-)$ 4.72 MHz. The simulated ENDOR transition at 2.66 MHz agrees well with the intersection $Y_{ACT}(+)$ 2.6. The rest of the simulated ESEEM transitions are very weak and are not either appear in the graphical method. The ENDOR transition at 3.68 MHz correspond best to the $X_{ACT}(+) = X_{ACT}(-)$ graphical intersections at 3.56 MHz, but they are in the limit of the accepted error. The low ENDOR frequencies at 1.08
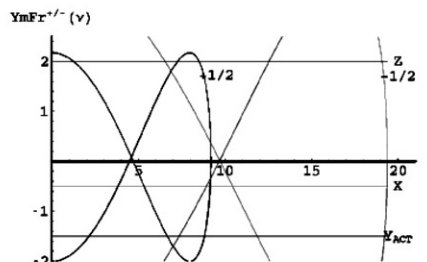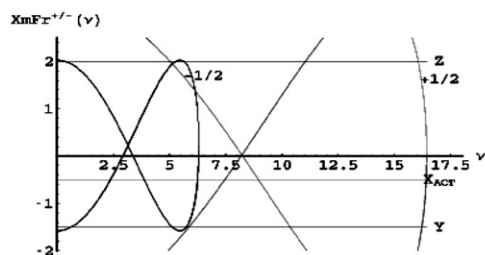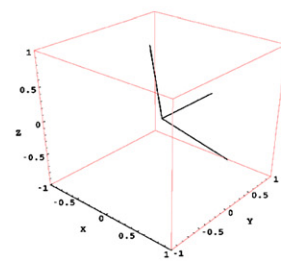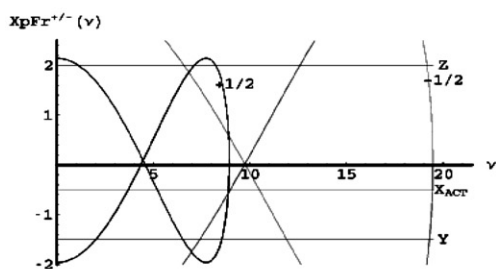
(m)
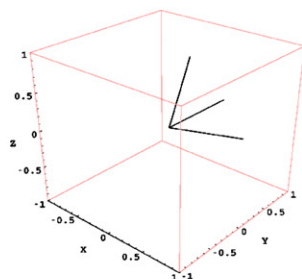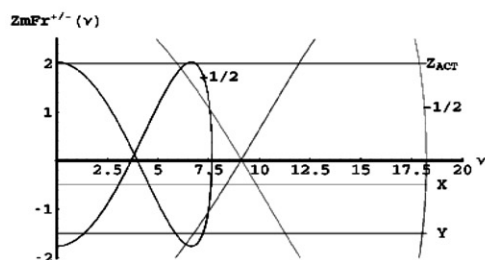
$M = 1/2$
Xa=(0.977, 0.0, 0.211)
Ya=(0.00, 1.00, 0.00)
Za=(0.277, 0.00, 0.961)
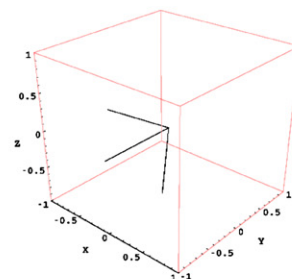
$M = -1/2$
Xb=(-0.996, 0.0, -0.0893)
Yb=(0.0, -1.00, 0.0)
Zb=(-0.0995, 0.00, -0.995)

(p)

$M = \mathbf{1/2}$; manifold alfa
Xa =(0.973, 0.0, -0.229)
Ya =(0.00, 1.00, 0.00)
Za =(-0.182, 0.0, 0.983}
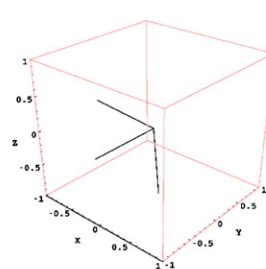
$M = -\mathbf{1/2}$; Manifold beta
Xb =(-0.996, 0.0, 0.0925)
Yb =(0.0, -1.0, 0.0)
Zb =(0.0836, 0.0, -0.997)
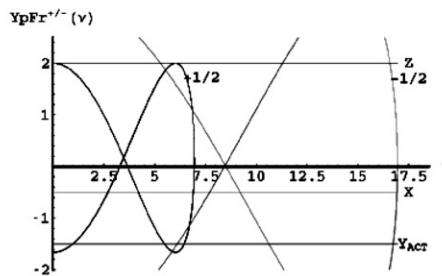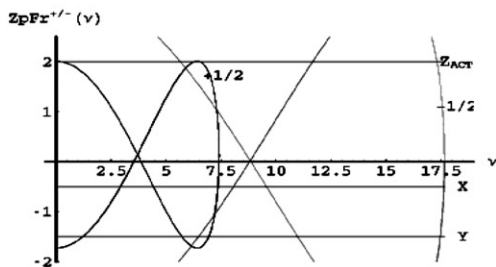
and 0.76 MHz do not correspond to any graphical intersection frequencies which are all too low, and generally the remaining intersections do not correspond to any simulated ENDOR or ESEEM frequencies. Generally speaking the graphical method in this case was not as good.

It is obvious that the *limiting dq* transitions $(v_{\lim})_{\max}$ were missing from the diagrammatic method because the characteristic directions are generally different from the "fourth characteristic direction." They must however be included to the values of the *characteristic dq frequencies* found by the intersections $F = f$ in the graphical solution. They comprise together the peaks found also in the spectral simulations.

11. Cancellation in the presence of the anisotropic hfi

For isotropic hfi, an important case analyzed in detail and used repeatedly for the interpretation of experimental spectra, is the case of *exact cancellation*. It can be achieved experimentally by adjusting the external magnetic field so that the value of the nuclear Zeeman frequency satisfies the condition $v_{0I} = |a|/2$, giving ENS frequency $|M a + v_{0I}| = 0$ in the *canceled manifold* and $2v_{0I}$ in the second one [11]. The orientation-independent ENSF value for isotropic hfi is exchanged by the magnitude $|\mathbf{v}_{I;M}|$ of the ENSF vector for anisotropic hfi. The variation of the magnitude of this vector with the field orientation practically eliminates the possibility of exact cancellation. The 3D plot of $|v_{I;M}|$ vs. the field orientation in Fig. 1 demonstrates that the ENSF for $M = 1/2$ becomes approximately zero in a limited subset of the field-orientation space, a line in the horizontal plane, where the *full cancellation condition* $\mathbf{v}_{I;M} = \mathbf{0}$ is satisfied.

At the points of full cancellation the linear combination of both the isotropic and the anisotropic part of the hfi for that particular orientation of the field cancel exactly the nuclear Zeeman. A zero value of $v_{I;M}$ can only be obtained in the rare (if not impossible) event that all the components of the ENSF vector vanish simultaneously. On the contrary the cancellation of the isotropic part of the hfi can be easily realized. This situation, i.e., $|a| = 2 |v_{0I}|$ in the anisotropic hfi case, has to be distinguished from the *full cancellation* $\mathbf{v}_{I;M} = \mathbf{0}$ and the *exact cancellation* in the isotropic hfi case. To point out the differences the employment of the particular name *cancellation of the isotropic part of the hfi* will be used further.

Some explicit results for the simple case described in the Appendix B, i.e., axial hfi and misalignment of the **Q** and **A** tensors $\Omega_A = (0, \beta, 0)$, could be derived for the field along the modified characteristic directions, according to Eq. (29). By a slight extension they reveal the influence of anisotropic hfi on the pure nq frequencies in the manifold where the isotropic part of the hfi cancels.

has been cancelled, i.e., for M such that $M a + v_{0I} = 0$. The allowed *dq* ESEEM transitions frequencies for the field along the modified characteristic directions follow in terms of the corresponding components of the ENSF vector under the square root, computed analytically for this limiting case.

$$v_1^{(X)} = 2\sqrt{v_X^2 + K^2(\eta + 3)^2/4} \quad \text{for } \mathbf{v}_{I;M} \| \mathbf{X} \text{ and } \mathbf{B}_0 \| \mathbf{X}',$$

$$\text{and } v_X(M) = \frac{\pm T\sqrt{2}}{\sqrt{5 + 3\cos 2\beta}}, \tag{41a}$$

$$v_2^{(Y)} = 2\sqrt{v_Y^2 + K^2(\eta - 3)^2/4} \quad \text{for } \mathbf{v}_{I;M} \| \mathbf{Y} \text{ and } \mathbf{B}_0 \| \mathbf{Y}',$$

$$\text{and } v_Y(M) = \pm T/2, \tag{41b}$$

$$v_3^{(Z)} = 2\sqrt{v_Z^2 + K^2\eta^2} \quad \text{for } \mathbf{v}_{I;M} \| \mathbf{Z} \text{ and } \mathbf{B}_0 \| \mathbf{Z}',$$

$$\text{and } v_Z(M) = \frac{\pm T\sqrt{2}}{\sqrt{5 - 3\cos 2\beta}}. \tag{41c}$$

The double sign indicates the dependence of the transition frequencies only on the magnitude of the perpendicular anisotropy T. The only sign requirement for the cancelled manifold M is $M a > 0$ for the normal nuclei with $v_{0I} < 0$.

Used for the system with the y-60° tilted **A**-principal frame compared to the **Q**-principal frame the Eqs. (41a)–(41c) give three new frequencies, $(v_{dq})_{X,\text{cancelled}} = 3.58$ MHz, $(v_{dq})_{Y,\text{cancelled}} = 2.55$ MHz, and $(v_{dq})_{Z,\text{cancelled}} = 1.14$ MHz, which are present in the simulated spectra of Fig. 7B (compare: 3.58, 2.6, and 1.18 MHz, respectively) for both $T = \pm 0.5$ MHz. The new frequencies differ very little from the pure quadrupole frequencies as it is obvious from the small contribution of the components of the ENSF vectors in the Eq. (41) for the present case of small axial anisotropy.

The analytical expressions for the frequencies of the non-cancelled manifold were too complicated to be practically useful, except for the Y' characteristic direction of the field in this particular limiting case. The following relation shows this component of $\mathbf{v}_{I;-M}$, which also gives a small contribution to the transition frequency for the present case.

$$v_Y(-) = 2v_{0I} + MT. \tag{42}$$

The peaks computed by this relation at (2.37, 1.87) MHz are detectable in the ideal ENDOR spectra but they are very weak.

Simulated three-pulse ESEEM and ideal ENDOR spectra of ^{14}N in doublets with anisotropic hfi and the scalar part cancelled are seen in Figs. 7A and B. The spectra consist in the four well-known lines of the isotropic case under exact cancellation conditions, the three relatively sharp peaks at the pure nq frequencies from the cancelled manifold and the *dq*-transition from the other manifold, which are slightly modified. The *dq* frequency at 5.57 MHz is well reproduced by
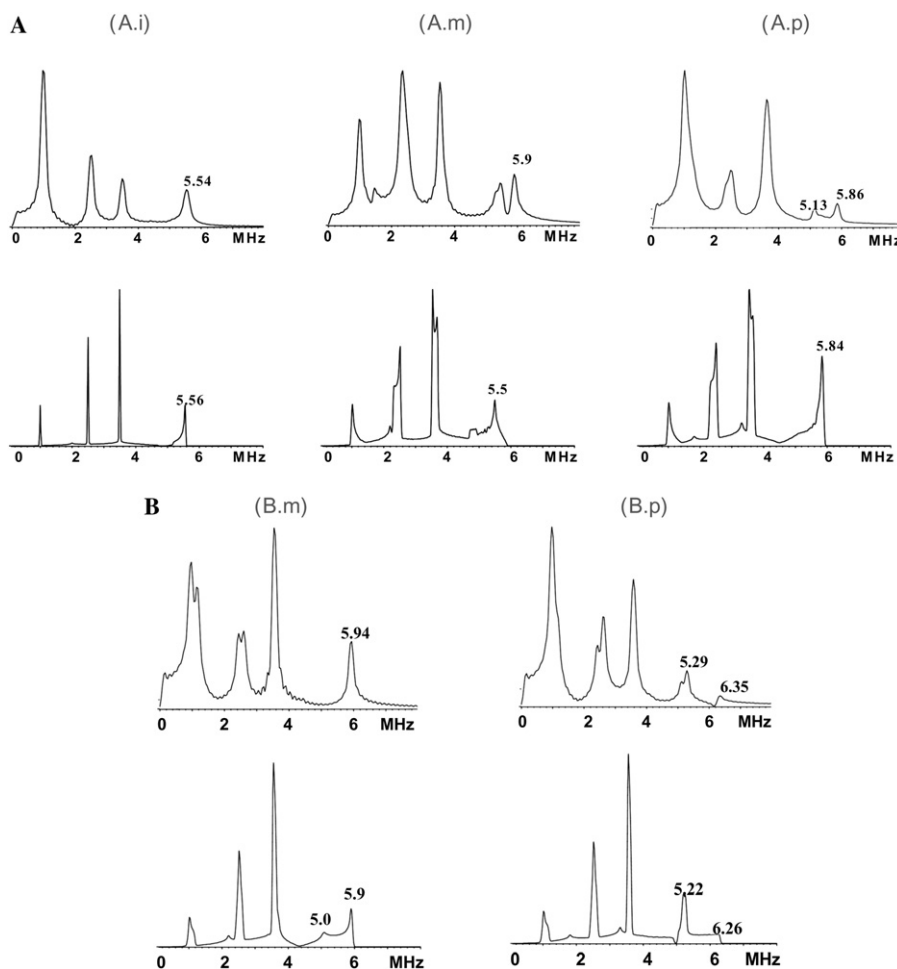
Fig. 7. (A) Ideal ENDOR and stimulated ESEEM ($\tau = 200$ ns) spectra simulated with the following parameters: $K = 1.0$ MHz, $\eta = 0.5$ resulting to $\mathbf{Q} = (-0.5, -1.5, 2.0)$ MHz; $|v_{0I}| = 1.06$ MHz, and $a = 2.12$ MHz. (a) $T = 0$; (m) $T = -0.5$ MHz or $\mathbf{A} = (2.62, 2.62, 1.12)$ MHz; (p) $T = 0.5$ MHz or $\mathbf{A} = (1.62, 1.62, 3.12)$ MHz. The traceless hfi-tensor $\mathbf{T}$ is defined as $(-T, -T, 2T)$. Coinciding nqi and hfi tensors. (i) ESEEM peaks: 5.53, 3.5, 2.5, 1.0; ENDOR peaks and steps: 5.56, 3.5, 2.5, 1.0. (m) ESEEM peaks: 5.9, 5.45, 5.29, 3.54, 2.36, 1.46, 0.977; ENDOR peaks and steps: 5.5, 4.8, 3.68, 3.56, 2.5, 2.36, 1.02. (p) ESEEM peaks: 5.86, 5.13, 3.62, 2.48, 2.3, 1.34, 1.01; ENDOR peaks and steps: 5.84, 5.1, 3.66, 3.56, 3.32, 2.5, 2.34, 1.82, 1.02. (B) ENDOR and ESEEM spectra calculated for the same parameter as in Fig. 6A but tilted $\mathbf{A}$ and $\mathbf{Q}$ principal frames with relative orientation of nqi and hfi tensors: (0, 60°, 0). (m) $T = -0.5$ MHz; (p) $T = 0.5$ MHz. (m) ESEEM peaks : 5.94, 3.54, 2.6, 2.44, 1.14, 0.977; ENDOR peaks and steps: 5.9, 5.0, 3.56, 2.52, 2.2, 1.14–1.02 (p) ESEEM peaks: 6.35, 5.29, 5.09, 3.58, 2.6, 2.44, 1.18, 0.977; ENDOR peaks and steps: 6.26, 5.22, 3.56, 2.54, 1.16–1.04. (All figures of the spectra are in MHz.)

$$v_{\lim,\pm} = 2\sqrt{4v_{0I}^2 + K^2(3 + \eta^2)}. \tag{43}$$

The anisotropy of the hfi may split the **dq** peaks of the ESEEM/ENDOR spectra or modify the shape of the **dq** peak to the powder type. It also may increase the width of the pure quadrupole transition peaks and split them in some cases.

In general, $v_{\lim}$ has maximum value $4\,v_{0I}$ when the nqi parameter K is small, while under full cancellation obtains the minimum value $(v_{\lim})_{\min} = 2K\,(\eta^2 + 3)^{1/2}$.

In ESEEM powders eventual **sq** peaks are located around the central frequency of definition of $F(v)$, $v = v_C$. The ability to detect the **sq** transitions in the spectrum is, however, inversely proportional to their width. Flanagan and Singel [11] derived an approximate

relation for the width of the **sq** transitions by Taylor expansion of F about the central frequency v_C. Using the notations of the present work the relation for the width of the single quantum transitions δv_{sq} would be transcribed to:

$$\delta\tilde{v}_{sq} = \frac{3(\eta + 3)\tilde{v}_{I;M}^2}{2(\tilde{v}_{I;M}^2 + \eta^2 + 3)}. \tag{44}$$

It is of interest here to investigate the near cancellation situation of the isotropic part for anisotropic hfi. The approximate width $\delta v_{sq} \approx 3(\eta + 3)(v_{I;M}/K^{1/2})^2/2$ $(\eta^2 + 3)$ computed in this case implies increasing broadening of the **sq** transitions for greater deviation from cancellation and/or decreasing K. In the opposite extreme where the transition frequencies are determined

by the nuclear Zeeman, i.e., for small quadrupole strength K and/or large hfi, the relation $\delta v_{sq} \approx 3(\eta + 3) K/2$ is obtained, which can be as much as 6 K and exceed the resonance frequency for the usual case of $v_{0I} \approx K$. Summarizing, both for a decrease of a large K and an increase of small K will broaden the *sq* transitions.

12. The graphical solution

The ESEEM and ENDOR spectral simulations for cancellation of the isotropic part of the hfi shown in Figs. 7A and B are compared with the graphical solution of the problem in Figs. 8 and 9. The chosen system had intermediate nqi strength with $|Kv_{0I}| \cong 0.94$ and the spectra here compare rather well to the corresponding isotropic case of Flanagan and Singel [11]. The deviation from the cancellation can be measured for the present scalar cancellation by the quotient $|Tv_{0I}| \cong 0.47$, which for isotropic hfi according Flanagan and Singel leads to a substantial destruction of the pure quadrupole triplet.

The conventional graphical method in the isotropic case (not shown) under cancellation displays very accurate values of the pure quadrupole peak positions 1.0, 2.5, and 3.5 MHz, and the *dq* peak at 5.56 MHz of the non-canceled manifold. However, the destruction of

the pure quadrupole triplet with the deviation from cancellation is not that serious in the present system. The basic isotropic peak structure of the simulated spectra remains almost unchanged for the anisotropic hfi, with small variations such as splitting and/or broadening of the peaks. This basic pattern agrees in the extended graphical method seen in Fig. 8(m) and (p). We note that the *anisotropy deviation* of the hfi $|T/a_{iso}| = 0.24$ for this example is double as much as in the first example of Figs. 4A and B but still rather small.

To facilitate the understanding of the diagrams two notes are in order.

(i) The graph of the partially cancelled manifold is the same for both $T = \pm 0.5$ MHz and the transition frequencies are consequently differentiated only by the non-cancelled manifold.

(ii) Only two distinct $F(v)$ curves, one for the perpendicular and one for the parallel orientation of the field to the unique symmetry axis of the **A**-tensor, exist in the present case due to the coinciding hfi and nqi tensors.

As seen in the diagram of the partially cancelled manifolds in Fig. 8(m) and (p) the median axes of the func-
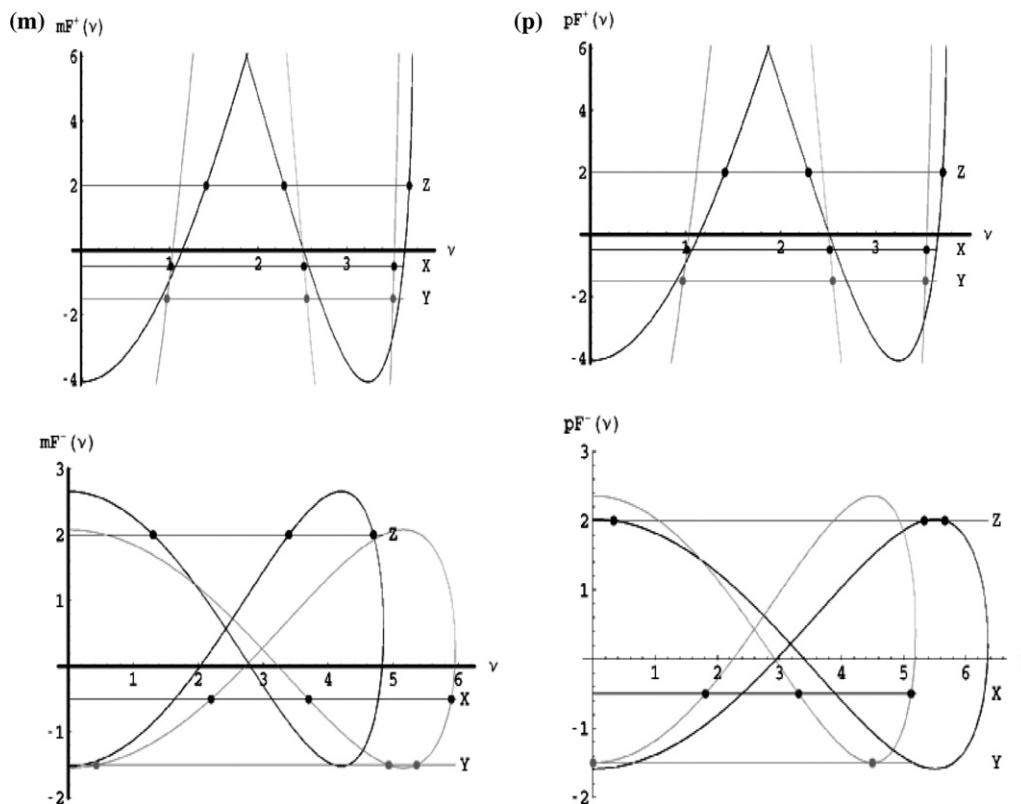

Fig. 8. The graphical solution for the axial hfi cases for the same system as in Fig. 7A. Only the intersections of the F curves with $f = 2$, $1 - \eta$, $-1 - \eta$, which are highlighted by the heavy points count as the solutions of the problem for the field along the principal **Q**-directions. Axial cases: (m) $T = -0.5$ MHz; (p) $T = 0.5$ MHz.

(m)
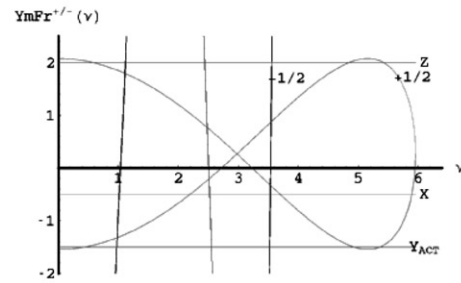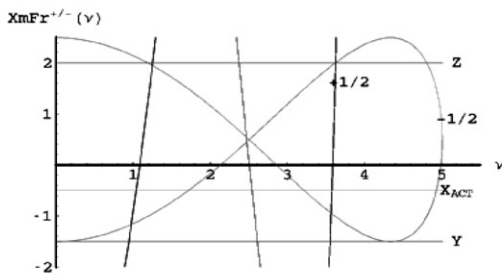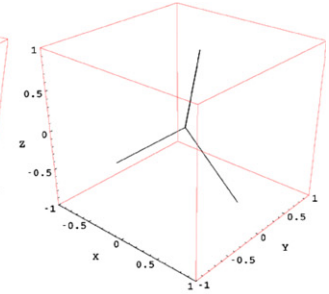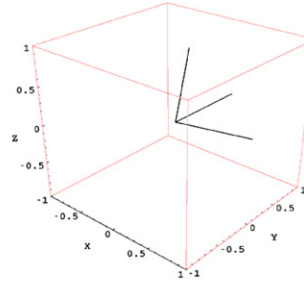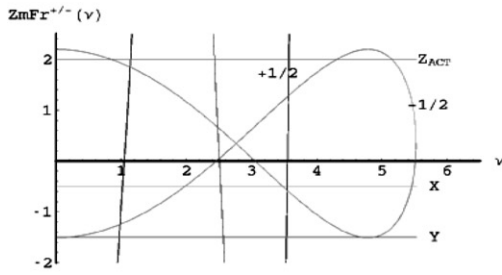
$M =1/2$
Xa =(0.989, 0.0, 0.147)
Ya =(0.00, 1.00, 0.00)
Za =(0.177, 0.0, 0.984)

$M =-1/2$
Xb =(0.189, 0.0, 0.982)
Yb =(0.0, −1.0, 0.0)
Zb =(0.721, 0.0, -0.693)

(p)

$M = 1/2$
Xb =(0.988, 0.0, −0.156)
Yb =(0.00, 1.00, 0.00)
Zb =(−0.132, 0.0, 0.991)

$M = -1/2$
Xb =(−0.190, 0.0, −0.982)
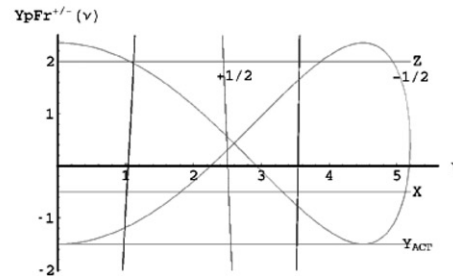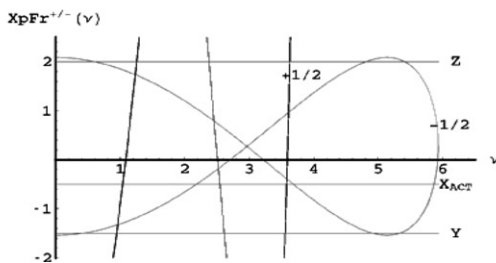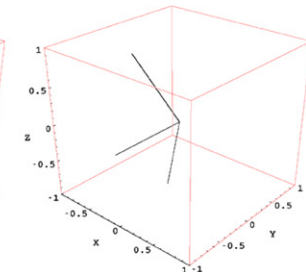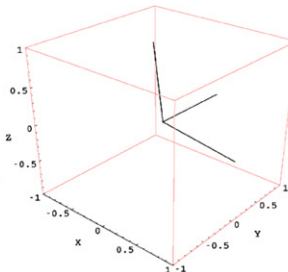Yb =(0.0, −1.00, 0.0)
Zb =(−0.721, 0.0, 0.693)
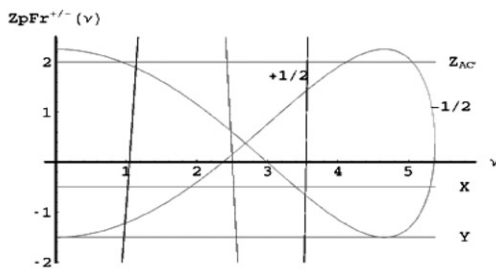

Fig. 9. The graphical solution for axial hfi for the same system as in Fig. 7B, but tilted **A**, **Q** principal axes by $\beta = 60°$. Only the intersections of the F curves with the horizontal lines $f(X_{ACT})$, $f(Y_{ACT})$ and $f(Z_{ACT})$ for which the field is along the modified characteristic directions count as solutions: (m) $T = −0.5$ MHz peaks: Z_{ACT} (1.2, 2.4, 3.55, **dq** = 5.1) MHz; X_{ACT} (1.0, 2.55, 3.65) MHz; Y_{ACT} (0.9, 2.55, 3.5, **dq** = 5.4) MHz. (p) $T = 0.5$ MHz peaks: Z_{ACT} (1.15, 2.35, 3.55, **dq** = 5.05) MHz; X_{ACT} (1.0, 2.55, 3.52, **dq** = 5.75) MHz; Y_{ACT} (0.9, 2.55, 3.5) MHz. The *limiting* **dq** transitions have to be computed separately, vide infra.

tions F are located rather high compared to $f(Z) = 2$, i.e., $F(v_C) > 2$. Thus, a weak orientation dependence of the transition frequencies is expected for this manifold, while the non-cancelled manifold displays substantial orientation dependence and corresponding disintegration of the *sq* peaks. In the latter case, the *dq* peaks are the only detectable transitions present at the value $v_{\lim}$ seen in Eq. (25). The *dq* transition can be furthermore split by the difference between the limiting frequencies in the parallel and the perpendicular direction.

As a complement to Fig. 9 where the graphical solution for tilted **A**-, **Q**-principal frames are given, two $(v_{\lim})_{\max}$ doublets at about (4.85, 5.95) MHz for $T = -0.5$ MHz, and (5.19, 6.36) MHz for $T = 0.5$ MHz were computed using Eqs. (38) and (39). It is obvious that the $(v_{\lim})_{\max}$ are missing from the diagrammatic method because the characteristic directions are generally different from the "fourth characteristic direction" corresponding to the *limiting dq* transition at $v_{\lim}$. These pairs together with the values of the characteristic frequencies in the graphical solution comprise together a good representation of the peaks found also in the spectral simulations of Fig. 7B.

13. Summary of results

(1) Analytical expressions of the ENS **g**-tensor $\mathbf{G}_M$ in the principal **Q**-frame and the ENSF vector components for the two sublevels $M = \pm 1/2$ under the influence of the hfi anisotropy, were derived.

(2) The ENSF vector $\mathbf{v}_{I;M}$, which has amplitude the ESEEM/ENDOR frequency before the consideration of nqi, could be expressed in terms of: (i) the scalar hf coupling a, (ii) the principal components of the **A**-tensor, (iii) the Euler angles Ω_A of the **A**-tensor with respect to the nqi, (iv) the polar and azimuthal angles (ϑ, φ) of the field direction with respect to the **Q**-principal frame, and (v) the nuclear Larmor frequency v_{0I}.

(3) The *stationary points* of the transition frequencies v were obtained with the ENSF vector $\mathbf{v}_{I;M}$ along the *principal orientations* with respect to the principal **Q**-frame, as in the isotropic hfi case.

(4) New field directions X', Y', and Z' corresponding to the above *stationary points* were defined as modified *characteristic directions*, deviating from the principal **Q**-tensor directions due to the hfi anisotropy. The new characteristic directions were obtained by using the $\mathbf{G}_M$ matrix.

(5) The *extreme/limiting values* of the function $f_M(\vartheta, \varphi; \Omega_g, \Omega_A)$ at the *stationary points* with respect to the field orientation (ϑ, φ) were exactly the same as in the isotropic hfi case, i.e. $-1 - \eta$, $-1 - \eta$, 2 for $\mathbf{v}_{I;M}$ along X, Y, and Z, respectively.

(6) The *maxima* in the absorption mode of the ideal ENDOR powders are expected to occur at the *stationary points* of f with the field along the corresponding characteristic direction. An additional stationary point giving a peak is expected in the ENDOR powders at the well-defined maximum frequency $v_{\max} = \sqrt{v_{I;M}^2 + K^2(\eta^2 + 3)}$. No characteristic direction of the field is expected for this max.

(7) The impact of the *cancellation condition* on the ESEEM spectra in the anisotropic case is expected to be generally smaller than in the isotropic case due to the *orientation dependent* ENSL frequency $v_{I;M}$ and the small probability of the *full cancellation* $v_{I;M} = 0$ only in very few orientations of the field. However, for small hfi anisotropy, cancellation of the isotropic part gives very similar spectral configuration as the exact cancellation in isotropic hfi systems.

14. Conclusion

The greatest obstacle in *generalizing* the *graphical method* to the powder spectra of polyoriented samples in systems with anisotropic hfi and/or **g**-tensor, is the dependence of the function F on the orientation of the field through the magnitude of the reduced ENSF $|v_{I;M}/K|$.

To cope with this problem, and actually expand the potential of the graphical method in delivering useful structural information even in the anisotropic case the following procedure can be used:

(i) Derivation of the modified orientations of the field for the three characteristic directions in the case of non-coinciding tensors and assignment of each one of them.

(ii) Computation of $|v_{I;M}|$ for each of the above directions.

(iii) Creation of separate 2D-plots of the F-function for each of the modified characteristic directions Z', X', and Y' of the field that contain also the straight horizontal lines corresponding to the limiting values of $f = 2$, $-1 + \eta$, and $-1 - \eta$, respectively.

(iv) Only the intersection $F_M(v) = f_M(U')$ for U' either X', Y', or Z' corresponding to the respective characteristic direction can be used to obtain the solutions and the characteristic features of the ideal ENDOR powders for the nuclear *sq* and *dq* transitions.

(v) The *limiting dq* transitions have to be treated separately at least for the tilted **A** and **Q** tensors, by analytical computation of the peaks using Eqs. (38) and (39), since there are not necessarily present in these diagrams.

One can suggest that the graphical approach modified for the case of the anisotropic hyperfine interaction can be used as useful supporting technique for the analysis and the simulation of the ESEEM/ENDOR powder spectra. The graphical approach provides direct information about all possible transition frequencies in these spectra that would help for the assignment of the questionable features in simulated and experimental spectra with final aim the determination of the hf and nq interactions.

Appendix A. The standard spherical transformation properties of the matrix **A**

The five standard spherical components of the *traceless part* $\mathbf{T}^{(2)}$ of the *symmetric tensor* $\mathbf{A}^{(2)}$ of *second rank*, e.g., the hfi tensor, are given in terms of the Cartesian components by the following relations:

$$\left.\begin{array}{l} T_{2;0} = \frac{1}{\sqrt{6}}[3A_{zz} - \mathrm{tr}(\mathbf{A})], \\ T_{2;\pm1} = \mp(A_{zx} \pm iA_{zy}), \\ T_{2;\pm2} = \frac{1}{2}(A_{xx} - A_{yy}) \pm iA_{xy}. \end{array}\right\} \tag{A.1}$$

The tensor $\mathbf{T}^{(2)}$ defined as $\mathbf{T}^{(2)} = \mathbf{A}^{(2)} - \mathrm{tr}\{\mathbf{A}^{(2)}\}/3$ is substantially simpler in its principal frame as seen in the following equation:

$$\left.\begin{array}{l} T_{2;0} = \frac{1}{\sqrt{6}}3T_{zz} = \sqrt{3/2}T_{zz}, \\ T_{2;\pm1} = 0; \quad T_{2;\pm2} = \frac{1}{2}(T_{xx} - T_{yy}). \end{array}\right\} \tag{A.2}$$

Using the above standard spherical tensor components of $\mathbf{T}$, the following equation gives the transformation of a component T_q from the principal $\mathbf{A}$-frame to the principal $\mathbf{Q}$-frame, [16].

$$\begin{aligned} T_q^{(2,Q)} &= \sum_{q'} T_{q'}^{(2,A)} D_{q'q}^{(2)}(\Omega_{QA}) \\ &= T_0^{(2,A)} D_{0;q}^{(2)}(\Omega_{QA}) + T_{\pm2}^{(2,A)}[D_{-2;q}^{(2)}(\Omega_{QA}) + D_{2;q}^{(2)}(\Omega_{QA})]. \end{aligned} \tag{A.3}$$

Eq. (13) which involves the Cartesian rotation matrix $\mathbf{R}$ is equivalent with the last equation but the application

of Eq. (A.3) is substantially simpler. The symbols D_{pq} are the matrix elements of the Wigner rotation matrix, found in any standard group-theory textbook. One has, however, to be careful with the correct sense of the Euler angles Ω_{QA} used in Eq. (A.3). For an *active rotation* of the tensor **A** from its principal frame to the new frame **Q**, by convention the Euler angles Ω_{QA} signify the inverse rotation of the principal coordinate frames **Q** to **A**, see [16].

Appendix B. Analytical treatment of limiting cases: axial A-tensor and tilt A, Q-axes

In this appendix the limiting case of *isotropic electron Zeeman* and *axial hfi tensor* will be studied analytically. To obtain transparent relations it will be assumed that the principal frame of the **A**-tensor is misaligned only by a rotation about the principal *Y*-axis of the **Q**-tensor by angle β. This angle will be the only parameter needed to specify the relative orientation of these tensors. In spite of this simplification, which means, $\Omega_{QA} = (\alpha, \beta, \gamma) = (0, \beta, 0)$, this system will allow the demonstration of some basic albeit interesting effects of the hfi anisotropy.

Starting with the general transformations of the Cartesian components T_{ij} of the hfi **A**-tensor to the **Q**-frame, and applying the *axial* hfi condition by eliminating the differences $T_{xx} - T_{yy}$ in Eqs. (15–17), and setting $\sin\alpha = \sin\gamma = 0$ and $\cos\alpha = \cos\gamma = 1$, one arrives to the following explicit expressions for the $\mathbf{G}_M$ matrix.

$$\mathbf{G}_M = \begin{pmatrix} G_M^{XX} & 0 & G_M^{XZ} \\ 0 & G_M^{YY} & 0 \\ G_M^{ZX} & 0 & G_M^{ZZ} \end{pmatrix}. \tag{B.1}$$

The non-zero matrix elements are for this case given as function of only the hfi parameter T, which is related with the traceless principal components of the hfi by $T = -T_\perp = T_\parallel/2$:

$$G_M^{(XX)} = M\left[a - \frac{T}{2}(3\cos2\beta - 1)\right] + v_{0I}, \tag{B.2a}$$

$$G_M^{(YY)} = M(a - T) + v_{0I}, \tag{B.2b}$$

$$G_M^{(ZZ)} = M[a + T(3\cos^2\beta - 1)] + v_{0I}, \tag{B.2c}$$

$$G_M^{(ZX)} = MT_{ZX} = \frac{3M}{2}T\sin(2\beta) = G_M^{(XZ)}. \tag{B.2d}$$

Application now for $\mathbf{B}_0 \parallel \mathbf{Z}$, gives the following ENS frequency vector.

$$v_{I;M}(\mathbf{B}_0\|\mathbf{Z}) \equiv \mathbf{G}_M \cdot \begin{pmatrix} 0 \\ 0 \\ 1 \end{pmatrix} = \begin{pmatrix} G_M^{(XZ)} \\ G_M^{(YZ)} \\ G_M^{(ZZ)} \end{pmatrix}$$

$$= \begin{pmatrix} \frac{3M}{2}T\sin(2\beta) \\ 0 \\ M[a + T(3\cos^2\beta - 1)] + v_{0I} \end{pmatrix}. \qquad (B.3)$$

The direction of the above vector $v_{I;M}$, which is lying in the XZ-plane, can be determined by the angle ϑ_M given in the following relation:

$$\tan\vartheta_M = \frac{v_{I;M}^{(X)}}{v_{I;M}^{(Z)}} = \frac{G_M^{(XZ)}}{G_M^{(ZZ)}} = \frac{\frac{3M}{2}T\sin(2\beta)}{M[a + T(3\cos^2\beta - 1)] + v_{0I}}. \qquad (B.4)$$

The characteristic directions of the field for a nuclear system depend only on the relative orientations on the **A**- and the **Q**-tensors, as it was shown in Eqs. (26)–(28) where the method of inversion of the $\mathbf{G}_M$ matrix for the determination of the *modified characteristic directions* was described. The inversion of the $\mathbf{G}_M$ matrix is a rather easy task for this simple limiting case. The direction of the new characteristic direction Z' is shown in the following equation:

$$\underline{Z}' \propto \begin{pmatrix} G_M^{(YY)} \cdot G_M^{(ZX)} \\ 0 \\ G_M^{(XX)} \cdot G_M^{(YY)} \end{pmatrix} \Rightarrow \tan\vartheta_{Z'} = \frac{Z_X'}{Z_Z'} = \frac{G_M^{(YY)} \cdot G_M^{(ZX)}}{G_M^{(XX)} \cdot G_M^{(YY)}} = \frac{G_M^{(ZX)}}{G_M^{(XX)}}. \qquad (B.5)$$

Substituting the matrix element of $\mathbf{G}_M$ we find the explicit expression,

$$\tan\vartheta_{Z'} = \frac{G_M^{(ZX)}}{G_M^{(XX)}} = \frac{\frac{3M}{2}T\sin(2\beta)}{M[a - \frac{T}{2}(3\cos 2\beta - 1)] + v_{0I}}. \qquad (B.6)$$

This characteristic direction lie in the XZ-plane. Two final expressions for the magnitude of the ENS frequency for well-defined angle β will be derived. (Notice that all the relations of this appendix can easily adapted to the cancellation of scalar part of the hfi by using $M a + v_{0I} = 0$.)

(a1) *Coinciding* **A**-, **Q**-*tensors*. Corresponds to $\beta = 0$ in Eq. (B.3).

For this case the $\mathbf{G}_M$ matrix becomes diagonal since the only off-diagonals $G_M^{(XZ)} = G_M^{(ZX)}$ vanish. This property results to ENSF vectors $v_{I;M}$ coaxial to the field when the field is parallel to any of the principal nqi axes. Accordingly, for the field in the Z-direction the following relation is obtained:

$$v_{I;M}(\mathbf{B}_0\|\mathbf{Z}) = \begin{pmatrix} 0 \\ 0 \\ M(a + 2T) + v_{0I} \end{pmatrix}. \qquad (B.7)$$

On the basis of Eq. (B.7) the magnitude of the ENSF vector in the Z-direction is given by:

$$|v_{I;M}^{(Z)}| = |M(a + 2T) + v_{0I}|. \qquad (B.8a)$$

Similarly, for the field along the transversal X and Y directions the following magnitude of the ENSF is obtained:

$$|v_{I;M}^{(X)}| = |M(a - T) + v_{0I}| = |v_{I;M}^{(Y)}|. \qquad (B.8b)$$

As the **A**-tensor is axial the field along both the transversal directions to Z gives the same ENSF vector.

(a2) A more general relation for the amplitude of the ENSF vector when the direction of the field is arbitrary can be obtained in the limiting case of *coinciding* **A**, **Q** *tensors*.

$$|v_{I;M}| = \sqrt{[M(a - T) + v_{0I}]^2 + 3MT[M(2a + T) + 2v_{0I}]\cos^2\vartheta}. \qquad (B.9)$$

This relation was tested in the plot of the Fig. 1.

(b) Let take now the more general relative **A**, **Q**-orientation with $\beta = 60°$.

We obtain $\sin 2\beta = (3)^{1/2}/2$ and $\cos 2\beta = -1/2$, giving:

$$v_{I;M}(\mathbf{B}_0\|\mathbf{Z}) = \begin{pmatrix} 3MT\frac{\sqrt{3}}{2} \\ 0 \\ M[a + T(3\frac{1}{4} - 1)] + v_{0I} \end{pmatrix}$$

$$= \begin{pmatrix} \frac{3\sqrt{3}M}{2}T \\ 0 \\ M(a - \frac{1}{4}T) + v_{0I} \end{pmatrix}. \qquad (B.10)$$

The final expression for the ENSF is given in this case by:

$$|v_{I;M}| = \sqrt{\frac{3^3}{2^4}T^2 + [M(a - \frac{T}{2^2}) + v_{0I}]^2}. \qquad (B.11)$$

Appendix C. The limiting-frequency transition v_{lim}

As opposed to the isotropic hfi case, each field orientation gives a different shape to the function F and the conditions for the solution v_{lim} of the secular equation are severely restricted. This solution corresponds to the very last point of the set of definition of the function $F(v)$ and can be obtained only when the *right-hand sides* of the following two expressions are equal:

$$F_M(\tilde{v}_{\text{lim}}) = \frac{2(1 - \eta^2)}{\tilde{v}_{I;M}^2}, \qquad (C.1)$$

$$f_M(\vartheta, \varphi) = -1 + \frac{3v_z^2 + \eta(v_x^2 - v_y^2)}{v_{I;M}^2}. \qquad (C.2)$$
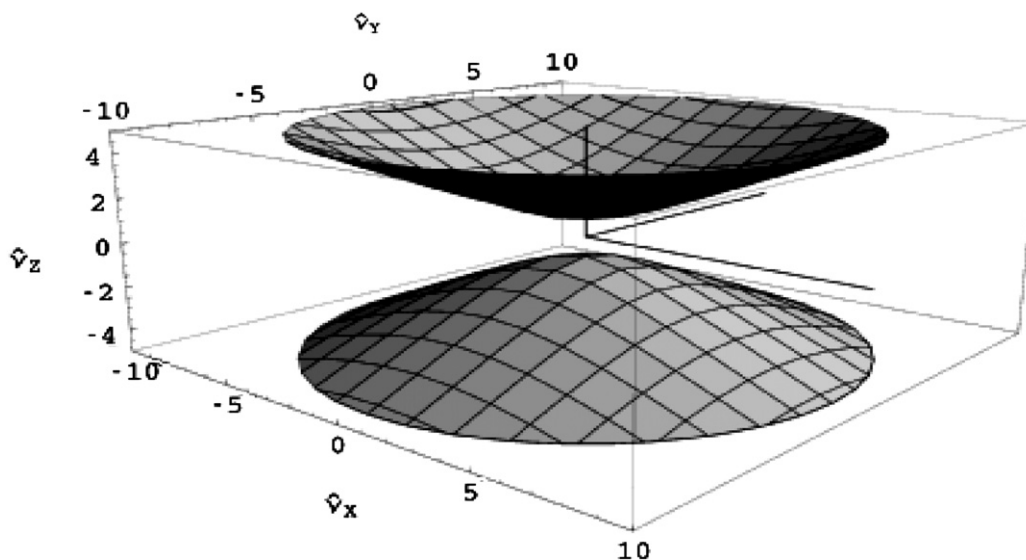
Fig. 10. Graphical representation of the *hyperboloid of two sheets* for the locus of the reduced ENSF vector $\tilde{v}_{I;M}$ computed according Eq. (40) for $\eta = 0.4$.

After some simple algebra the following relation was obtained for the components of the reduced ENSF vector $\mathbf{v}_{I;M}$.

$$\frac{\tilde{v}_Z^2}{(1-\eta^2)} - \frac{\tilde{v}_X^2}{2(1+\eta)} - \frac{\tilde{v}_Y^2}{2(1-\eta)} = 1. \qquad (C.3)$$

This equation defines the locus of the tip of the $\mathbf{v}_{I;M}$ vector which is a *hyperboloid of two sheets* circumventing the Z axis, as the one seen in Fig. 10. The $\mathbf{v}_{I;M}$ vector is subjected of course to additional conditions, such as finite length, depending on the case. The minimum length of $\mathbf{v}_{I;M}$ is given by $v_Z = K(1-\eta^2)^{1/2}$ which is obtained when the vector $\mathbf{v}_{I;M}$ is parallel to the Z axis, and is equivalent to $F(v_{\lim}) = 2$.

References

[1] A.J. Hoff (Ed.), Advanced EPR. Applications in Biology and Biochemistry, Elsevier, Amsterdam, 1989.

[2] B.M. Hoffman, V.J. DeRose, P.E. Doan, R.J. Gurbiel, A.L.P. Houseman, J. Telser, Metalloenzyme active-site structure and function through multifrequency CW and pulsed ENDOR, Biol. Magn. Reson. 13 (1993) 151–218.

[3] J. Hüttermann, ENDOR of randomly oriented mononuclear metalloprotein: toward structural determination of the prosthetic group, Biol. Magn. Reson. 13 (1993) 219–252.

[4] Y. Deligiannakis, M. Louloudi, N. Hadjiliadis, Electron spin echo envelope modulation (ESEEM) spectroscopy as a tool to investigate the coordination environment of metal centers, Coord. Chem. Rev. 204 (2000) 1–112.

[5] A. Schweiger, G. Jeschke, Principles of Pulse Electron Paramagnetic Resonance, Oxford University Press, New York, 2001.

[6] G.M. Muha, Exact solution of the NQR $I = 1$ eigenvalue problem for an arbitrary asymmetry parameter and Zeeman field strength and orientation, J. Chem. Phys. 73 (1980) 4139–4140.

[7] G.M. Muha, The Zeeman effect in spin = 1 systems, J. Magn. Res. 49 (1982) 431–443.

[8] S.A. Dikanov, Yu.D. Tsvetkov, M.K. Bowman, A.V. Astashkin, Parameters of quadrupole coupling of ^{14}N nuclei of chlorophyll a cations determined by electron spin method, Chem. Phys. Lett. 90 (1982) 149–153.

[9] A.V. Astashkin, S.A. Dikanov, Yu.D. Tsvetkov, Modulation effects from ^{14}N and ^{15}N nuclei in the electron spin echo of imidazoline nitroxyl radicals containing the 2-oximinoalkyl group, J. Struc. Chem. 25 (1984) 45–55.

[10] P. Kottis, R. Lefebvre, Calculation of the electron spin resonance line shape of randomly oriented molecules in a triplet state. I. The $\Delta m = 2$ transition with a constant linewidth, J. Chem. Phys. 39 (1963) 393–403.

[11] H.L. Flanagan, D.J. Singel, Analysis of ^{14}N ESEEM patterns of randomly oriented solids, J. Chem. Phys. 87 (1987) 5606–5616.

[12] H.-I. Lee, P.E. Doan, B.M. Hoffman, General analysis of ^{14}N ($I = 1$) electron spin echo envelope modulation, J. Magn. Res. 140 (1999) 91–107.

[13] A.G. Maryasov, M.K. Bowman, HYSCORE Spectra for paramagnetic centers with nuclear spin 1 having isotropic HFI, J. Phys. Chem. B 108 (2004) 9412–9420.

[14] N.P. Benetis, A.R. Sørnes, Automatic spin-hamiltonian diagonalization for electronic doublet coupled to anisotropic nuclear spins applied in one- and two-dimensional ESE simulations, Conc. Magn. Res. 12 (6) (2000) 410–433.

[15] N.P. Benetis, P. Dave, D. Goldfarb, Characteristics of ESEEM and HYSCORE spectra of higher electron-spin multiplets (S > 1/2) in orientationally disordered systems, J. Magn. Res. 158 (2002) 126–142.

[16] D.M. Brink, G.R. Satchler, Angular Momentum, Clarendon Press, Oxford, 1968.

[17] A.M. Tyryshkin, personal communication: *Ideal ENDOR* simulation program, based on exact solution of the two sublevel spin Hamiltonians ($I > 1/2$). The effect on the transition probabilities of relative orientation of the rf field B_2 compared to B_0 in the spatial averaging is included but the "hyperfine enhancement" and relaxation effects are ignored.